3 Pressure Dependence of the HOONO/HONO$_2$ Branching Ratio in the Reaction OH+NO$_2$+M; Pulsed Laser Photolysis Studies

3.1 Introduction

The reaction of the reactive hydroxyl (OH) and nitrogen dioxide (NO$_2$) radicals to produce the stable molecule nitric acid (HONO$_2$) plays a critical role throughout the atmosphere. The yield of nitric acid from this reaction is reduced due to a competing minor channel producing peroxynitrous acid (HOONO).

$$\mathrm{OH} + \mathrm{NO_2} + \mathrm{M} \xrightarrow{k_{1a}} \mathrm{HONO_2} + \mathrm{M} \qquad \text{Reaction 3.1a}$$

$$\mathrm{OH} + \mathrm{NO_2} + \mathrm{M} \xrightarrow{k_{1b}} \mathrm{HOONO} + \mathrm{M} \qquad \text{Reaction 3.1b}$$

An introduction to the importance of these reactions in the atmosphere can be found in chapter 1.

Appendix A describes the absorption spectroscopy of HOONO and first direct measurement of the branching ratio k_{1b}/k_{1a}. This was my first project as a graduate student. While those results were a significant contribution to our understanding of reaction 3.1, the discharge flow method used to generate OH radicals suffered some significant drawbacks: (1) the impact of collisions with the reactor wall and secondary chemistry were unknown, (2) the gas composition was predominantly He and therefore did not reflect our atmosphere, and (3) measurements could only be made at pressures below 40 torr. As a result, while the branching ratio measured with the discharge-flow apparatus help constrain the HOONO yield in the low-pressure limit, the yield under conditions relevant to the lower atmosphere remained highly uncertain.

3.1.1 HOONO: What Do We Know?

HOONO has been a molecule of considerable interest to the physical chemistry community over the past two decades. This stems from the potential atmospheric impact of a significant HOONO yield, but also from the complexity the multiple conformers and intramolecular hydrogen bond give to its potential energy surface and spectroscopy. As a result, HOONO has now been studied from many different angles: *ab initio* calculations, condensed phase spectroscopy [40-43], gas phase vibrational spectroscopy (fundamental and overtones, jet cooled and room temperature), rotational spectroscopy, biexponential OH + NO_2 kinetics, and statistical rate modeling.

Taking the literature data set as a whole, portions of the ground state potential energy surface connecting OH + NO_2, $HONO_2$, HOONO, and HO_2 + NO can now be described in considerable detail (Figure 3.1). Unless otherwise specified, all stated energies are relative to OH + NO_2.

The most accurate measurement of the HOONO binding energy comes from the jet-cooled action spectroscopy conducted in Marsha Lester's group at the University of Pennsylvania. By measuring the overtone spectrum of *trans-perp* HOONO and the internal energy of the OH dissociation fragments, they measured the dissociatioin energy of *trans-perp* HOONO to be -16.2±0.1 kcal mol^{-1} [44].

The dissociation energy of *cis-cis* HOONO has also been estimated experimentally. Matthews and Sinha, working with *cis-cis* HOONO at room temperature, measured the OH rotational distributions using action spectroscopy. From this, they measured D_0 (*c-c*) = -19.9±0.5 kcal mol^{-1} [45]. In a similar experiment, McCoy et al. found the OH quantum yield in the action spectroscopy of the *cis-cis* HOONO $2\nu_1$

band to be consistent with D_0 (*c-c*) = -19.6 kcal mol^{-1} [46]. In a very different experiment, Hippler et al. analyzed observed bi-exponential OH decays to derive equilibrium constants for *cis-cis* HOONO. From this they estimated D_0(*c-c*) = -19.2±0.5 kcal mol^{-1} [47]. *Ab initio* calculations of the *cis-cis* HOONO dissociation energy, even at high levels of theory, vary from 18.4 to 19.8 kcal mol^{-1} [48-51]. These calculations are further complicated by errors in the calculated enthalpies of OH and NO_2. A more consistent and accurate *ab initio* result is the energy of the *trans-perp* isomer relative to *cis-cis* HOONO, calculated to be $\Delta H^0(0) = 3.4$ kcal mol^{-1} [7, 51]. This can be combined with the measured *trans-perp* dissociation energy to yield D_0 (*c-c*) = -19.6 kcal mol^{-1}.

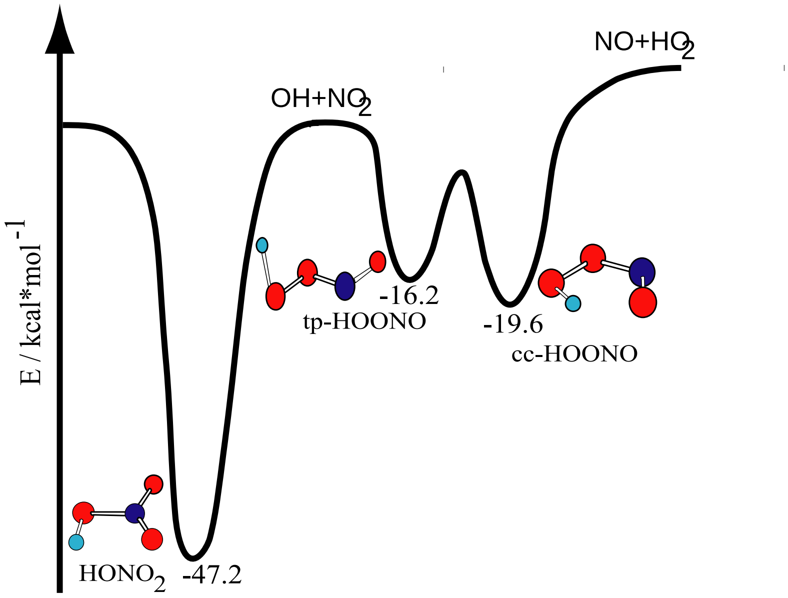

Figure 3.1. Potential energy surface for the reaction of OH + NO_2 + M. Energies are in reference to OH + NO_2 and corrected for zero-point energy. *trans-perp* HOONO energy from Konen et al. [44]. *cis-cis* HOONO energy from calculated ΔH(0) relative to *trans-perp* HOONO.

One prolonged debate in the HOONO community has surrounded the possible third stable conformer, *cis-perp* HOONO. While initial *ab initio* predicted this geometry to be a stable conformer [52] subsequent calculations at higher levels of theory indicated that the *cis-perp* HOONO minimum may [51] or may not [7, 49] be a stable minimum on the potential energy surface. Infrared spectra of HOONO trapped in Ar matrices by Y. P. Lee's group contained bands corresponding to *trans-perp* and *cis-cis* HOONO, but not *cis-perp* [43]. While *cis-perp* HOONO is likely not a stable minimum on the potential surface, there is considerable evidence that *cis-perp*-like geometries are accessed through the torsional excitation of *cis-cis* HOONO [45, 46, 53, 54]. This will be discussed in more detail in Section 3.1.3.

The only experimental determination of the *trans-perp* to *cis-cis* isomerization barrier was made by measuring the temperature-dependent disappearance of *trans-perp* HOONO using overtone action spectroscopy [55]. This barrier was measured to lie 7.9±2.9 kcal mol^{-1} above *trans-perp* HOONO; in agreement with *ab initio* calculations of 9.6-10.8 kcal mol^{-1} [49, 52, 55-57]. The *trans* to *cis* isomerization barrier is thus 6-7 kcal mol^{-1} below the dissociation energy and so the dominant fate of *trans-perp* HOONO should be isomerization to the *cis-cis* conformer.

It should be noted that a recent RRKM master equation modeling study has challenged this conclusion, suggesting that instead *trans-perp* HOONO may have a concerted mechanism to isomerize preferentially to nitric acid [58]. It was hypothesized that a low-energy barrier was necessary to account for recent experimental observations of nitric acid formation from the reaction HO_2 + NO. *Ab initio* studies have consistently been unable to find such a low-energy transition state. Calculalted transition states for concerted isomerization of *trans-perp* HOONO to $HONO_2$ instead lie 12.5-14 kcal mol^{-1} above the barrier for isomerization to *cis-cis* HOONO (1.5-3 kcal mol^{-1} above dissociation to OH + NO_2) [48, 56, 57].

With the potential energy surface shown in Figure 3.1, we can begin to tell the story of the reaction 3.1. The initial interaction forms both [HOONO]* and $[HONO_2]^*$ with considerable internal energy. Under atmospheric conditions, most of these nascent molecules re-dissociate before they can be stabilized by collisions with a third body. Due to its larger binding energy, $[HONO_2]^*$ has a longer lifetime and reaction 3.1a dominates. At higher pressures, as the rate of collisions with a third body increases, the relative HOONO yield will increase.

Collisionally stabilized [HOONO]* initially fall into the wells corresponding to the various HOONO conformers. At very low (200 K) temperatures, these various conformers can be stable long enough to be observed. At room temperature, however, all HOONO molecules are predicted to isomerize to the lowest-energy *cis-cis* conformer on the timescale of ≈300 μs even at 20 torr [7, 55].

Cis-cis HOONO then undergoes unimolecular decomposition back to $OH + NO_2$ with a time constant on the order of 1 s in the lower troposphere. Because HOONO is likely to be re-dissociate to OH and NO_2 and has a much shorter lifetime than $HONO_2$, production of HOONO by reaction 3.1b reduces the efficiency of reaction 3.1 to sequester HO_x and NO_x. This leads us back to our need to know the branching ratio for reaction 3.1 under atmospheric conditions.

There have been several previous measurements and calculations of the branching ratio, but only at conditions quite removed from those found in the atmosphere. At very high temperatures and pressures the HOONO dissociation lifetime is much shorter. This has been observed in the form of bi-exponential OH decays by the Hippler and Hynes groups [47, 59, 60]. These decays can then be fit to extract the rate constants k_{1a} and k_{1b}

as well as the equilibrium constant K_{1b}. Hippler et al. measured $k_{1b}/k_{1a} = 0.15$ at 430 K and 5 bar He, with a HOONO dissociation rate of 20 μs [60]. D'Ottone et al. measured $k_{1b}/k_{1a} = 0.10 \pm 0.03$ at 413 K and 400 torr He, with a HOONO dissociation rate of 200 μs [59].

At lower temperatures, there have also only been a few estimates of the branching ratio, all at very low pressures. Donahue et al. measured the rate of ^{18}OH scrambling in the OH + NO_2 reaction. From this, they estimated the branching ratio in the low-pressure limit to be $k_{1b}/k_{1a} = 0.17$ [61]. Nizkorodov and Wennberg in their first spectroscopic detection of HOONO estimated a HOONO yield of 5±3% at 253 K and 20 torr [62]. The only direct measurement of the reaction 3.1 branching ratio remains those made by cavity ringdown spectroscopy as described in appendix A [7]. The published branching ratio has been revised (see section 3) to $k_{1b}/k_{1a} = 0.048 \pm 0.013$ at 298 K and 14 torr. While not a laboratory experiment, a recent time-dependent capture theory calculation produced a branching ratio of $k_{1b}/k_{1a} = 0.051$ at 20 torr and 300 K and produced a similar temperature-dependence to that shown in our early discharge-flow experiments [63].

Several studies have calculated values of the branching ratio [47, 49, 58, 63-67]. Early calculations, either pure RRKM calculations or RRKM calculations modified to fit the existing data, produced widely varying estimates of the branching ratio at 1 atm: >1% [66], 2.5% [67], and 30% [65]. More recent calculations that take advantage of the more detailed knowledge of the potential energy surface and new additions to the kinetics data set, are more consistent. The results of Golden et al. and Hippler et al. along with other branching ratio determinations below 1 atm are shown in Figure 3.2. We see that, with the exception of the Donahue et al. value, the qualitative agreement is reasonable, but there remains a dearth of experimental data on the branching ratio in this pressure range.

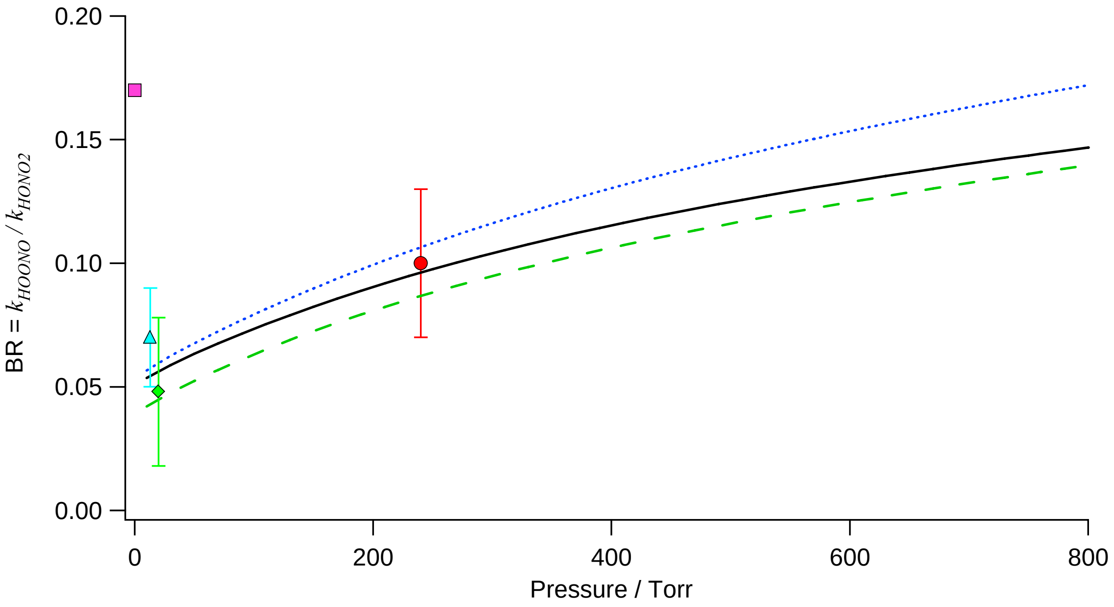

Figure 3.2. Calculated and measured values of the branching ratio below 1 atm. Hippler (green dashed line), Golden (dotted line), the JPL 2006 recommendation (solid line), Donahue (pink square), Nizkorodov (green diamond), D'Ottone (red circle), and Bean (blue triangle). Experimental pressures from Bean and D'Ottone have been scaled to reflect an effective N_2 pressure. No corrections have been made for temperature.

The NASA-JPL 2006 kinetics data evaluation (also shown in Figure 3.2) recommends rate constants that yield branching ratios between those of Golden and Hippler. The IUPAC kinetics data evaluation still contains no recommendation for the inclusion of reaction 3.1b.

3.1.2 Branching Ratio Pressure Dependence

It was shown in Bean et al. that *cis-cis* HOONO can be detected using infrared cavity ringdown spectroscopy (CRDS) [7]. The infrared spectra of HOONO and $HONO_2$ can then be used to measure the branching ratio k_{1b}/k_{1a}. Those measurements were limited to low pressures by the microwave discharge used to generate OH radicals. Thus, the main challenge in extending branching ratio measurements to higher pressures was the development of a method for the generation of OH radicals at pressures up to 1 atm. This was accomplished through the use of a coupled laser photolysis-CRDS apparatus.

OH radicals were produced by the photolysis of ozone to produce excited-state oxygen atoms $O(^1D)$ in the presence of hydrogen or methane. After allowing complete reaction with NO_2, IR spectra of the products were recorded with CRDS. The branching ratio was then measured by integrating the ν_1 OH-stretch bands of *cis-cis* HOONO and $HONO_2$ and converting these to product concentrations with *ab initio* ratio of cross sections.

By generating OH radicals through laser photolysis, reaction 3.1 could be initiated over a wide range of pressures up to 1 atm. While the generation of product by photolysis decreased our overall signal by reducing the sample path length, this technique had several major advantages over microwave discharge: (1) Products were measured in a mostly nitrogen environment, more closely resembling the atmosphere. (2) Products were probed shortly after they are produced (100 μs) to minimize the influence of secondary chemistry. (3) Products were formed and probed in the center of the cell, minimizing the impact of wall reactions. (4) The product spectrum and the background were collected simultaneously, eliminating uncertainty due to changes in mirror properties. The most significant advantage of the laser photolysis method, however, is that it allowed access to a much wider range of pressures.

We therefore measured the pressure-dependence of the HOONO yield from reaction 3.1 from 20 to 760 torr and report the first measurement of the HOONO yield from reaction 3.1 at 1 atm.

3.1.3 Stretch-Torsion Coupling

A critical step in our branching ratio measurements was the integration of the *cis-cis* HOONO ν_1 band. This was accomplished by fitting the observed product spectrum with reference spectra for HOONO, HONO, and $HONO_2$. The reference spectrum used to fit the *cis-cis* HOONO band is shown in Figure 3.3. This spectrum was generated during the discharge-flow studies by subtracting the $2\nu_2$ bands of *cis*- and *trans*-HONO from the observed product spectrum [7]. The HONO subtraction on the blue side was difficult and, for lack of a better option, the spectral profile used for integration was assumed to be linear for the R-branch edge. The resulting band shape was clearly asymmetric, with appreciable intensity spread to the blue.

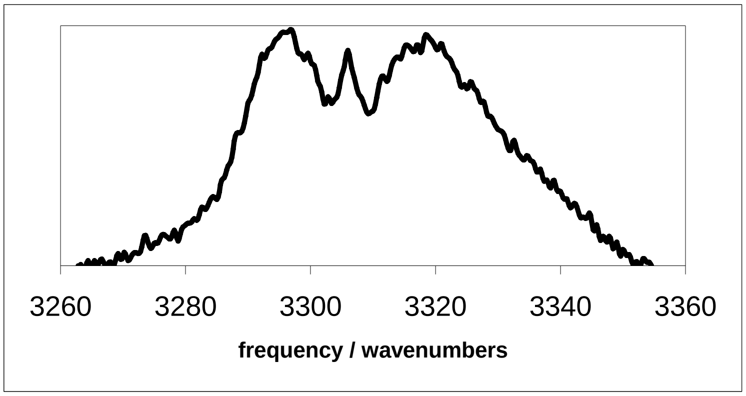

Figure 3.3. *Cis-cis* HOONO spectrum used to fit experimental data.

Originally, the blue shading in the spectrum was assumed to be the result of two processes: (1) intramolecular hydrogen bond tightening in the vibrationally excited state leading to a more compact geometry and slightly larger upper state rotational constants and (2) population in low-frequency vibrational modes such as the *a″* HOON torsion (ν_9), the *a″* ONOO torsion (ν_8), and the *a′* NOO bend. In particular, excitation of the HOON torsion would be expected to break the intramolecular hydrogen bond and lead to substantially shifted sequence bands. Any shifts in spectral intensity larger than 30-40 cm^{-1} would have been obscured by spectral interference of the HONO and $HONO_2$ bands. As a result, we were concerned that *cis-cis* HOONO integrated absorbance obtained with the spectral shape shown in Figure 3.3 may under-represent the total $\nu_1=1\leftarrow0$ absorption.

As mentioned above, the coupling of the OH stretch to the HOON torsion has been studied previously [45, 46, 54, 68]. The action spectrum of the $2\nu_1$ band of *cis-cis* HOONO has an unusual shape, with a large amount of intensity in bands blue-shifted from the band origin. The blue-shifted bands could be understood through coupling of the HOON torsion to the OH stretch. The overtone spectrum was simulated by calculating the two-dimensional *ab initio* potential energy and dipole moment surfaces for *cis-cis* HOONO as functions of the HOON torsional angle and OH bond length. The calculated minimum-energy potential as a function of the HOONO torsional angle showed a shelf that opened up about 700 cm^{-1} above the zero-point energy (Figure 3.4). This shelf leads to a pileup of torsional states in the 700-800 cm^{-1} energy region. The wave functions of these states lead to geometries with the OH predominantly out of the plane. As a result, $2\nu_1$ transitions from these excited torsional states lead to absorptions that are significantly blue-shifted and more intense than absorptions from the ground state.

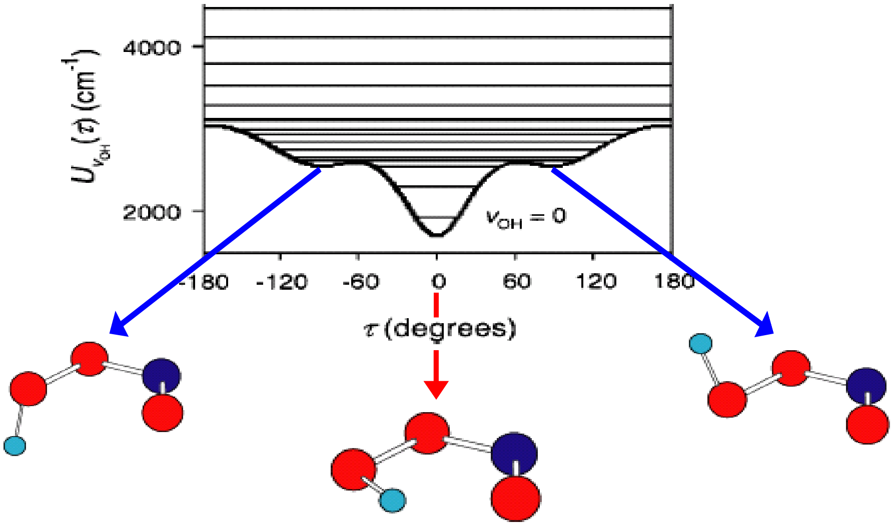

Figure 3.4. Vibrationally adiabatic potential energy surface as a function of the HOON torsion angle. The location of ν_9 states are shown as lines. Adapted from [46].

The two-dimensional calculations also yielded a predicted spectrum for the ν_1 fundamental. The impact of this shelf upon the fundamental OH stretch was predicted to be much less than that for the overtone, but still led to a prediction that 25% of the *cis-cis* HOONO absorption intensity may be blue-shifted outside of our reference spectrum. These calculations only considered one of the low-frequency modes of *cis-cis* HOONO. To better understand the positions and frequencies of important sequence bands, we felt it necessary to repeat these calculations including both low-frequency torsional modes.

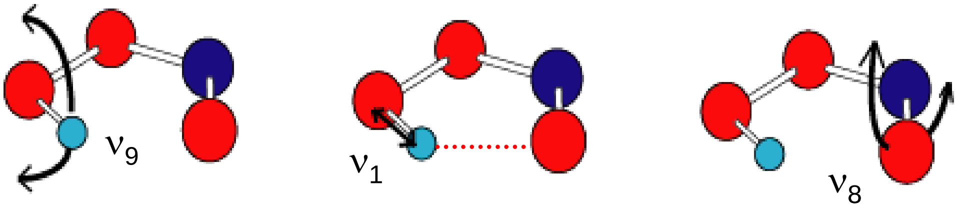

Figure 3.5. *cis-cis* HOONO vibrational bands: OH stretch (ν_1), HOON torsion (ν_9) and ONOO torsion (ν_8). The intramolecular hydrogen bond (red dashed line) red-shifts the OH stretch.

If we picture the most stable planar *cis-cis* HOONO geometry and the HOON and OONO torsional motions (Figure 3.5) we would expect both torsions to influence the intramolecular hydrogen bond and for the two modes to be coupled. Additionally the two-dimensional results of McCoy et al. and Matthews et al. agree qualitatively but obtain different energies for the lowest HOON torsional state. McCoy et al., who froze the ONOO into a planar arrangement, calculate 382 cm^{-1}, while Matthews et al, who let the heavy atoms relax in their calculations, calculate 290 cm^{-1}. This is a fairly large difference, indicating that the heavy atoms have a significant impact on the details of the HOONO potential and the OH stretch.

To better understand the influence of the two torsional modes and their coupling on the fundamental OH stretch spectrum of *cis-cis* HOONO, we calculated the 3D *ab initio* potential energy surface for HOONO surrounding the *cis-cis* minimum as functions of the HOON torsional angle (ν_9), ONOO torsional angle (ν_8), and OH bond length (R_{OH}). By calculating a potential energy surface of HOONO with enough detail, we aimed to derive the energies of the low-frequency torsional modes associated with the $v_1=0$ and $v_1=1$ states to the highest accuracy possible. From these energies the frequencies and relative intensities of sequence bands can be calculated and the *cis-cis* HOONO absorption intensity that falls outside our assumed band shape can be calculated and corrected for.

In support of these calculations, we also re-measured the HOONO spectrum. With improved HONO and $HONO_2$ reference spectra, we have tried to resolve spectral features corresponding to torsionally excited HOONO transitions.

3.2 Experimental Methods

3.2.1 Generation of Reactants

Spectra were taken in a reaction flow cell combining UV excimer laser photolysis for production of radicals and IR-CRDS for the detection of products. A schematic of the experimental apparatus is shown in Figure 3.6.

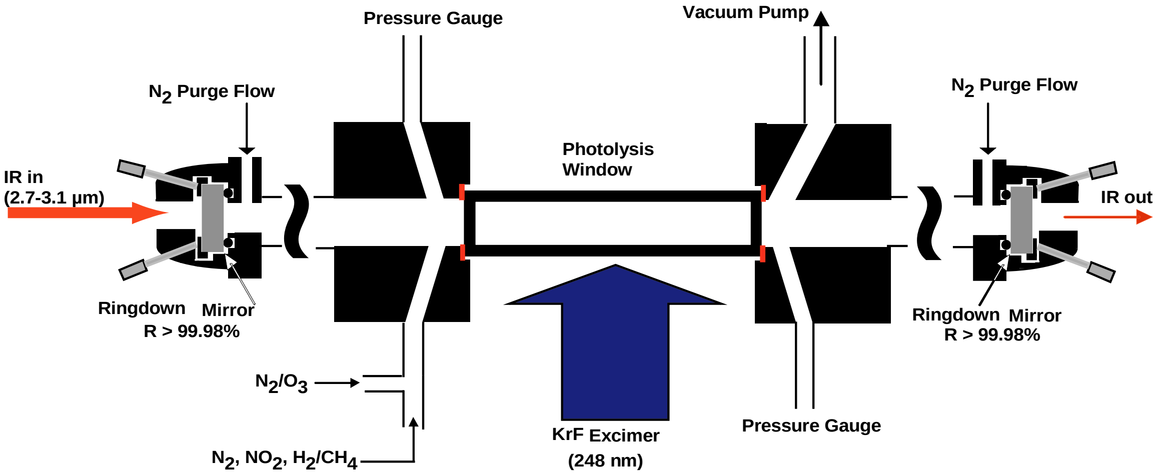

Figure 3.6. Photolysis/CRDS flow cell. Length of the photolysis cells were 3.6, 6.0, and 12.0 cm. Typical photolysis beam width was 2 mm.

The design uses a rectangular photolysis cell coupled on both ends to Teflon blocks. These blocks provide feed throughs for gas inputs, a pump out port and pressure gauges, and they serve to link the photolysis cell to the ringdown mirrors. Dimensions and assembly of the photolysis cells are described in appendix B. We initiated the reaction $OH + NO_2 + M$ via the following reaction scheme.

$O_3 + h\nu(248\text{ nm}) \rightarrow O(^1D) + O_2$ Reaction 3.2
$O(^1D) + H_2 \rightarrow OH + H$ Reaction 3.3
$H + NO_2 \rightarrow OH + NO$ Reaction 3.4
$OH + NO + M \rightarrow HONO + M$ Reaction 3.5
$OH + NO_2 + M \rightarrow HONO_2 + M$ Reaction 3.1a
$\rightarrow HOONO + M$ Reaction 3.1b

While this overall reaction scheme was an efficient and clean way to make OH with few unwanted by-products, it required a system free of O_2 to prevent the rapid formation of HO_2 from the H atoms produced in reaction 3.3. As a result, the branching ratio measurements were all done in a gas mixture of mostly N_2 (>90%) with the remainder essentially all H_2.

While these measurements could not be carried out in air, the branching ratio is not expected to have a significant dependence upon the nature of the bath gas. In particular, the lack of O_2 in our gas mixtures should have a minimal effect on the branching ratio due to the similar collision efficiencies, β, of N_2 and O_2. The presence of a significant fraction of H_2 in our measurements does impact the branching ratio, due to the much lower collision efficiency of H_2. A first-order correction for this was made by calculating an effective pressure for each experiment,

$$P_{\text{effective}} = P_{\text{baratron}} \times \left(f_{\text{N}_2}\beta_{\text{N}_2} + f_{\text{H}_2}\beta_{\text{H}_2} \right),$$

where f_{N2} and f_{H2} are the fractions of total flow consisting of N_2 and H_2 respectively. For this calculation we assumed the collision efficiency for H_2 to be that given by Golden et al. for He, $\beta_{H2}/\beta_{N2}=0.4$ [49]. This correction had the largest impact on data taken at low pressures, when the fraction of H_2 was highest.

Both reaction 3.3 and reaction 3.4 are known to produce OH with a high degree of vibrational excitation. As a result, some experiments were carried out with the OH production from the reaction

$$O(^1D) + CH_4 \rightarrow OH + CH_3. \qquad \text{Reaction 3.3b}$$

It was assumed that the collision efficiency of CH_4 was the same as for N_2.

Ozone was delivered to the cell by flowing nitrogen through silica gel saturated with ozone. Ozone was generated by an ozonizer (Osmonics V10-0) and collected by flowing through a U-tube containing silica gel (6-12 mesh) kept at -78 ^{0}C. Silica gel saturated with ozone turned deep purple. Filling the trap could be accomplished in under an hour. Ozone was then delivered to the cell by flowing nitrogen through the silica gel trap still at -78 ^{0}C. The trap was always kept at about 1 atm with a needle valve after the trap. The ozone concentration would stabilize after 10-15 min as an equilibrium between ozone diffusion within the silica gel and the nitrogen flow was established. If the flow through the trap and the cold bath were left undisturbed, a constant flow of 300 sccm containing about 1×10^{17} molecules$\times$cm^{-3} could be sustained for over 12 hours. To prevent ozone from reaching our mechanical pump, an ozone scrubber was inserted into the vacuum line. The scrubber consisted of approximately two feet of 1-inch tubing filled with copper mesh and heated to >100 ^{0}C.

Hydrogen and methane were introduced as pure gas flows. NO_2 was introduced as a 4% mixture in nitrogen (Matheson). All reactant gases and a nitrogen dilution flow were mixed in a glass cross about 5 cm from the photolysis region. All gas flows were through mass flow transducers (Edwards Model 831 and Omega Model 1700) calibrated volumetrically so that final concentrations in the photolysis cell could be calculated. Typical concentrations used for the pressure-dependent measurements are listed in Table 3.1.

Table 3.1. Concentrations used in HOONO/HONO$_2$ branching ratio measurements.

Gas	Concentration range / molecules×cm^{-3}
O_3	(1-10)×10^{15}
NO_2	(1-10)×10^{16}
H_2 / CH_4	(1-10)×10^{17}
N_2	balance to pressure

Photolysis was initiated with the 248 nm pulse from a KrF excimer laser. The output beam was a slightly diverging 1 cm × 2.5 cm rectangle. The excimer beam was sent through a +50 cm focal-length cylindrical lens and -30 cm focal-length circular lens such that the beam entering our cell matched the width of our photolysis window on the long axis of the beam and 2-5 mm along the short axis. The laser flux was varied over the range 1-50×10^{15} photons cm^{-2} to test for any possible dependence of the measured branching ratio on the photolysis energy.

3.2.2 Detection of Products

Absorption spectra of the reaction products were recorded by pulsed cavity ringdown spectroscopy. The details of our CRDS apparatus have been described in detail in Chapter 1 and will only be described briefly here. A mid-infrared laser pulse (2.7-3.3 μm) was injected into an optical cavity made by two high-reflectivity infrared mirrors (R=99.98%). Spectra of reaction products were typically recorded by scanning the spectral region of interest alternating 16 shots with the excimer on and then 16 shots with the excimer off and then subtracting the two. This subtraction eliminated background due to species present in the absence of reaction, as well as to the wavelength-dependent ringdown loss of the mirrors. By comparing the ringdown lifetime with and without the photolysis laser, the absorbance of the photolysis products was measured,

$$A = \frac{L_{cav}}{c}\left(\frac{1}{\tau_{\text{Photolysis}}} - \frac{1}{\tau_0}\right),$$

with a minimum-detectable absorbance of $A = 10^{-6}$. The frequency of the infrared laser was then scanned over the fundamental v_1 (OH stretch) spectral region to obtain the partially rotationally-resolved spectra of HOONO (3306 cm^{-1}) and $HONO_2$ (3350 cm^{-1}) as well as the by-product nitrous acid (HONO, 3275 cm^{-1} and 3370 cm^{-1}). The production of HONO from reaction 3.6 was unavoidable, but did not impact our ability to integrate the HOONO and $HONO_2$ spectra.

It should be stated that, unlike the absolute measurements described in Chapter 2, these experiments only require accurate *relative* absorbances. The mirror-to-mirror length and path length occupied by the sample therefore did not influence our results since these values were the same for both HOONO and $HONO_2$. As a result, data analysis was conducted using the raw data values of $1/\tau$ rather than the true absorbance. Where appropriate, data will be shown in units of “absorbance per pass,” but this was an unnecessary step that was omitted in the general data analysis.

3.2.3 3D Potential and Energy Levels

These calculations have primarily been the work of Matthew Sprague and Anne McCoy and will only be described briefly here. Optimized geometries and energies were calculated by Sprague at various geometries using the GAUSSIAN98 and 2003 programs [69]. A 3D potential energy surface was computed in two steps. First a fully-optimized

2D surface over the HOON torsional angle (τ_9) and OONO torsional angle (τ_8) was computed in which the torsional angles were held fixed while all other angles and all bond lengths were allowed to relax. Second, for each pair of torsional angles, single-point energy calculations were run at various values of the OH bond length.

In order to decrease the time required for each calculation, the geometries were optimized in a sequence of progressively more costly levels of theory and basis sets. The initial optimization was done with Møller-Plesset perturbation theory truncated at second order with correlation consistent polarized double ζ basis set (MP2/cc-pVDZ). The geometry from this calculation was then re-optimized at coupled cluster doubles level of theory with the same basis set (CCD/cc-pVDZ) and then re-optimized again at coupled cluster with singles and doubles with perturbative triples level of theory (CCSD(T)/cc-pVDZ), and again with the larger consistent polarized triple ζ basis set (CCSD(T)/cc-pVTZ). This final geometry was then used for energy calculations done at the CCSD(T)/cc-pVTZ level of theory/basis set.

These calculations were run at many different geometries to generate a two-dimensional minimum energy potential as a function of τ_9 and τ_8. Since the final level of theory was the same as used in McCoy et al., their results for $\tau_8=0°$ were used. The values of τ_9 and τ_8 were selectively chosen to help map out critical areas of the potential with a minimum of points, as the calculations were quite time consuming. For each optimized geometry, single-point energy calculations were carried out as the OH bond length (R_{OH}) was varied about its minimum-energy length (R_{min}). R_{OH} was varied from R_{min}-0.15 Å to R_{min}+0.25 Å at 0.05 Å intervals. All other angles and bond lengths were held constant and the calculations were performed at the same CCSD(T)/cc-pVTZ level of theory as the final geometry optimization.

All of the calculated energies were then given to Anne McCoy for further analysis. The single-point energies were used to calculate a three-dimensional analytical potential energy surface, fitting to an expansion of the three coordinates, τ_9, τ_8, and R_{OH}, 79 terms in all. The R_{OH}-dependence was expressed as a quartic expansion in $(1-\exp(-\alpha * \Delta R_{OH}))$; the angular dependence was fit to a high-order expansion in $\left(1-\cos\tau\right)$ and the explicit HOON torsion dependence of the effective mass associated with the HOON torsion as a function of R_{OH} was included.

McCoy then used this three-dimensional potential energy surface to solve the Schrödinger equation in the vibrationally adiabatic approximation, separating ν_1 from ν_8 and ν_9, to obtain the frequencies of the torsional states of *cis-cis* HOONO with ν_1=0, ν_1=1, and ν_1=2. The wave functions associated with each of these states were also generated.

This study has not yet been finished. Several calculations of energies and the final 3D potential energy surface remain incomplete. While the results presented here should be treated as preliminary, they include all of the points that will be calculated near the bottom of the well. Since the Botzmann correction factor derived below is dominated by these states, I expect the future refining of the potential energy surface to have only a small impact on this result.

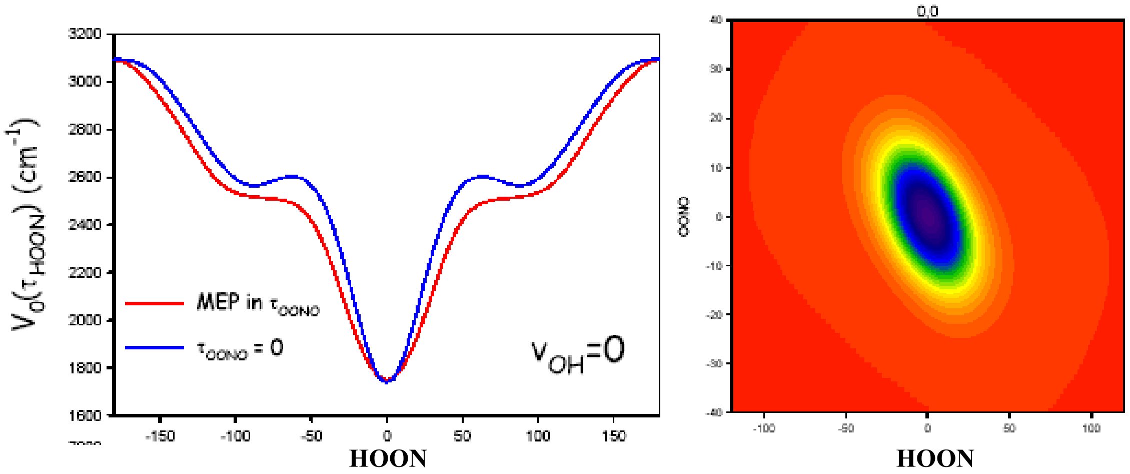

Figure 3.7. The 2D potential energy surface for HOONO as a function of the OONO (vertical) and HOON(horizontal) torsional angles. Red is high energy and purple is low. The 1D potential of the HOON torsion along the minimum-energy path is also shown and compared to the 1D potential obtained with the OONO torsion fixed at 0.

The ground state wavefunction and the one-dimensional adiabatic potential along the minimum energy path are shown in Figure 3.7. We see that the two torsional modes are clearly coupled, leading to a shift in the ground state wave function to lie along the diagonal between the two torsions (this effect is exaggerated by the plot shown, since the axes are on different scales). We see that the one-dimensional potential along the minimum energy path is significantly wider and has its shelf at slightly lower energy than that obtained by holding the OONO torsion at 0. The expected result of this is that the ν_9 states will be shifted to lower energy and the pileup of states at the shelf will also be at slightly lower energy.

The calculated frequencies for the two states of interest to our measurements, ν_1=0 and ν_1=1 are shown in Table 3.2. The assignments were made based on the wavefunctions and the average kinetic energy of each torsion.

Table 3.2. Calculated torsional states of *cis-cis* HOONO. The relative ground-state populations at 298 K and the ν1=0→1 transition frequencies associated with each state are also shown. Energies and frequencies are both given in cm^{-1}.

		$\nu_{OH}=0$			$\nu_{OH}=1$			
n-HOON	**n-OONO**	**energy**	**E-ZPE**	P_{Rel}	**energy**	**E-ZPE**	**transition freq**	**blue shift**
0	0	2174.19	0.00	1.000	5546.25	0.00	3372.06	0.00
1	0	2481.65	307.45	0.227	5897.99	351.74	3416.35	44.29
0	1	2659.93	485.74	0.096	6046.14	499.89	3386.21	14.15
2	0	2687.65	513.46	0.084	6174.41	628.16	3486.76	114.71
3	0	2767.79	593.60	0.057	6314.99	768.74	3547.19	175.14
4	0	2827.44	653.25	0.043	6396.30	850.05	3568.86	196.80
5	0	2924.94	750.75	0.027	6472.36	926.11	3547.42	175.36
1	1	2940.52	766.33	0.025	6358.44	812.19	3417.92	45.86
6	0	3022.74	848.55	0.017	6572.06	1025.81	3549.32	177.26
2	1	3094.61	920.42	0.012	6611.61	1065.36	3517.00	144.94
0	2	3122.12	947.92	0.010	6529.22	982.97	3407.10	35.04
7	0	3132.87	958.68	0.010	6679.30	1133.05	3546.43	174.37
3	1	3163.90	989.71	0.008	6712.07	1165.83	3548.17	176.11
3	2	3229.19	1055.00	0.006	6771.08	1224.83	3541.88	169.82
8	0	3237.30	1063.11	0.006	6794.21	1247.96	3556.91	184.85
	?	3319.54	1145.35	0.004				
9	0	3343.60	1169.41	0.004				
	?	3379.65	1205.46	0.003				
	?	3412.30	1238.11	0.003				
	?	3422.77	1248.58	0.002				

I have used these frequencies to generate a simulated room temperature spectrum of the *cis-cis* HOONO OH-stretch coupled to the two torsional modes. Frequencies of transitions from levels containing quanta in ν_8 or ν_9 were obtained by comparing the frequencies of these states in $\nu_1=0$ and $\nu_1=1$. The Boltzmann populations of these states were calculated to weight the various transitions. The populations and frequencies were then combined to generate a simulated spectrum and calculate what percentage of the ν_1 band was blue-shifted outside of the HOONO spectrum used for fitting.

A careful experimental investigation of the HOONO band profile was also conducted to search for features characteristic of torsionally excited HOONO. Three scans were taken covering the range 3245-3445 cm^{-1} in 0.2 cm^{-1} step sizes. Scans were taken at 250 torr and room temperature. An attempt was made to minimize the HONO produced by reducing the concentrations of H_2 and O_3 and increasing the concentration of NO_2.

3.2.4 Vibrationally Excited OH

The possible influence of vibrationally excited OH (OH*) on the HOONO branching ratio measurements was a concern. OH produced from both reactions 3a and 4 are known to produce OH*. While collisional deactivation of OH* is fairly efficient collisions of hot OH with NO_2 undoubtedly occur. NO_2 is known to be an efficient quencher ($k = 4.8\times10^{-11}$ cm^3 $molecule^{-1}$ s^{-1}) for excited OH [70].

$$OH^* + NO_2 \rightarrow OH + NO_2^* \qquad \text{Reaction 3.6}$$

In two cases the presence of OH* would not concern us. If the only result of reaction 3.6 is quenching, then nitric acid and HOONO are only produced from OH + NO_2 and clearly the branching ratio we measure is not influenced by OH*. If some of our measured product does result from OH* + NO_2 + M, but the branching ratio is unaffected by the vibrational excitation, then again this would not influence our result.

If, however, a significant fraction of our measured products does come from OH*,

$$OH^* + NO_2 + M \rightarrow HONO_2 + M, \qquad \text{Reaction 3.7a}$$

$$OH^* + NO_2 + M \rightarrow HOONO + M, \qquad \text{Reaction 3.7b}$$

then reactions 3.7a and 3.7b compete with reactions 3.1a and 3.1b. If the branching ratio is not the same as for these two sets of reactions, perhaps favoring the more stable nitric acid product in reactions 3.7, then our measured branching ratio may be influenced by the degree of OH vibrational excitation. Experimentally, we have tried to address this by altering the initial OH* distribution and by adding an efficient quencher.

We varied the initial OH* distribution by switching our OH generation from reaction 3.3a and reaction 3.4 to reaction 3.3b. While $O(^1D)$ + CH_4 also produces OH*, the yield with $\nu > 2$ is less than from reaction with H_2 [71, 72]. A careful examination of our observed HOONO/$HONO_2$ yields over the full pressure range showed no correlation between the source chemistry and the branching ratio.

We also tried to investigate the role of OH* by introducing an efficient quencher. SF_6 is the classic quencher for vibrational excitation due to its large mass and number of vibrational modes. The introduction of SF_6 to our experiments should increase the rate of OH* quenching and increase the percentage of our product coming from reaction of NO_2 with OH in the ground state. A series of branching ratio measurements were made at 330 torr at concentrations of SF_6 in the range $[SF_6] = (0\text{-}7.5)\times10^{15}$ cm^{-3}. All other conditions such as precursor concentrations and excimer power were kept constant during the experiment. A clear trend was seen in the ratio of HOONO to $HONO_2$ areas with $[SF_6]$ as shown in Figure 3.8.

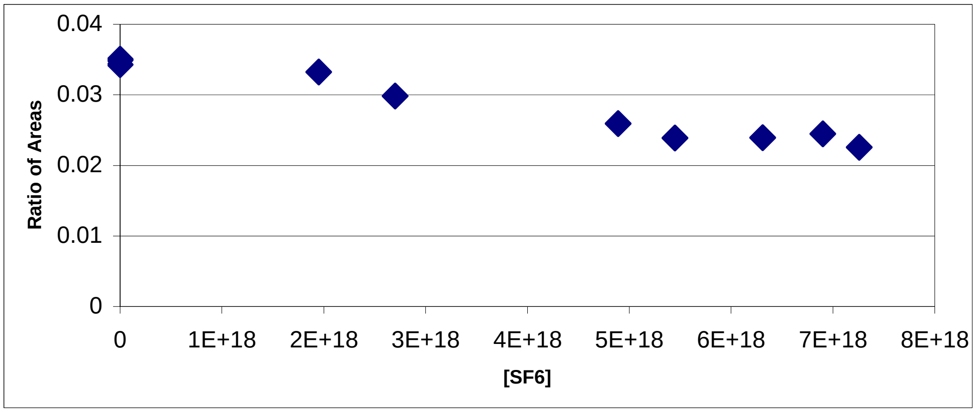

Figure 3.8. Ratio HOONO/$HONO_2$ areas measured at 300 torr total pressure as a function of SF_6 concentration.

While the presence of SF_6 clearly decreased the HOONO/$HONO_2$ ratio, the trend was opposite what we would expect if this was due to changes in the OH vibrational-state distribution. An increase in $[SF_6]$ should increase the rate of quenching for hot OH. If this impacts the branching ratio at all, I would expect a reduction in hot OH to increase formation of the more weakly bound HOONO product.

The stronger evidence that this trend with $[SF_6]$ is unrelated to vibrationally hot OH is in the raw HOONO and $HONO_2$ areas shown in Figure 3.9. If the presence of SF_6 was influencing the branching ratio, we would expect the two to trend in opposite directions. Instead, the HOONO absorbance remains constant, while the nitric acid absorbance increases steadily with $[SF_6]$. This is indicative of a change in CRDS detection of nitric acid and is likely the result of a change in the pressure broadening of the nitric acid band by SF_6. This was supported by observed changes in the observed nitric acid band shape at higher [SF_6] also indicative of pressure broadening. The impact of pressure broadening on the CRDS detection of nitric acid is discussed in detail in chapter 2.

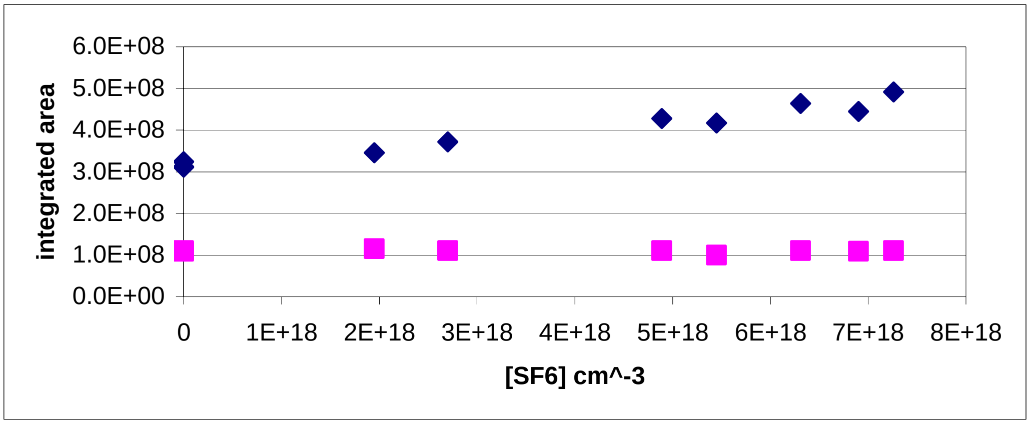

Figure 3.9. Integrated areas of HOONO (pink squares) and $HONO_2$ (blue diamonds) measured at 300 torr as a function of SF_6 concentration. The HOONO integrated areas have been multiplied by 10 to be on the same scale.

This large change in the nitric acid area makes interpreting the branching ratio data in Figure 3.8 with respect to the role of OH vibrational excitation difficult. The most reliable data is the HOONO area as a function of [SF_6] shown in Figure 3.9. From this, we cconclude that there is no evidence that adding SF_6 to the cell impacted the production of HOONO in our cell.

In summary, we have tried to evaluate the possible influence of OH* on our branching ratio measurements in two ways: changing the initial vibrational distribution of OH and adding an efficient quencher. Neither experiment showed evidence of a change in the HOONO yield. This result seems to indicate that the influence of OH* on the branching ratio is not large, but does not prove the lack of influence. Conclusive proof would require a method for generating uniformly cold OH without introducing large spectral interference in our detection region.

3.2.5 Branching Ratio Measurements

Several steps were involved in measuring the branching ratio from reaction 3.1: (1) measuring the infrared spectrum of the reaction products, (2) fitting the data spectrum with reference spectra, (3) integration of the ν_1 bands of HOONO and $HONO_2$, (4) correcting measured integrated absorbances for known errors, and (5) conversion from relative absorbance to relative concentrations using the ratio of *ab initio* calculated cross sections.

Excimer on-off spectra collected as described in Section 3.2.2 were then fit with reference spectra of all known bands in the region of interest: HOONO (3306 cm^{-1}), $HONO_2$ (3350 cm^{-1}), HONO (3260 cm^{-1}, 3372 cm^{-1}, and 3590 cm^{-1}) and, formaldehyde (3472 cm^{-1}, only when CH_4 was used as an OH precursor). The ν_1 bands of HOONO and $HONO_2$ in their respective reference spectra were then integrated:

$$\int Abs_{\mathrm{HOONO}} = \int_{3250\ \mathrm{cm}^{-1}}^{3370\ \mathrm{cm}^{-1}} \left(\frac{1}{\tau} - \frac{1}{\tau_0} \right) d\nu \,,$$

$$\int Abs_{\mathrm{HONO_2}} = \int_{3480\ \mathrm{cm}^{-1}}^{3620\ \mathrm{cm}^{-1}} \left(\frac{1}{\tau} - \frac{1}{\tau_0} \right) d\nu \,.$$

Errors in the measured $HONO_2$ and HOONO absorbances were then corrected. As described in detail in Chapter 2, the correction factor in nitric acid absorbances stems from nonlinearities in the CRDS spectra: $E_{\mathrm{HONO_2}} = \frac{A_{\mathrm{CRDS}}}{A_{\mathrm{True}}}$. The magnitude of this correction factor was highly pressure dependent and ranged from 0.4 at 20 torr to 0.85 at

1 atm. A correction factor for our HOONO integrated absorbances was introduced to account for blue-shifted intensity from torsionally excited HOONO. This correction factor, f_{Boltz}, was derived from the calculated Boltzmann population of torsional states as described in Section 3.3.3.

In order to convert from the integrated absorbances of the two species to relative concentrations, we rely on calculations of the ratio of their integrated absorption cross sections. When calculating ratios, significant cancellations of systematic errors occur when comparing similar vibrations. Even in calculations we have done in the harmonic approximation comparing nitric acid and peroxynitrous acid, despite errors in absolute intensities of nearly a factor two, the calculated ratios agreed with experiment within 20% [7]. We have been collaborating with Professor John F. Stanton on calculations of HOONO and related species. He has completed a high-level (CCSD(T)/ANO) calculation of the full quartic force field of $HONO_2$ and of all isomers of HOONO within the second-order vibrational perturbation theory (VPT2). For small molecules with nearly complete basis sets these calculations have been found to be robust [73, 74]. The $HONO_2$ intensities for ν_1 and $2\nu_2$ from these calculations as well as all HOONO and $HONO_2$ frequencies agree with experiment to better than 5%, giving us considerable confidence in the calculated ratio of intensities: $I_{\text{HONO2}}/I_{\text{HOONO}} = 2.71$.

Table 3.3. Comparison of HOONO and $HONO_2$ frequency and intensity calculations.

		Harmonic	Harmonic	Anharmonic	Experiment
		CCSD(T)/ AUG-cc-pVTZ Francisco	CCSD(T)/ ANO Stanton	CCSD(T)/ ANO Stanton	
HOONO					
	ω_1, cm^{-1}	3521	NA	3320	3306[a]
	$2\omega_1$, cm^{-1}	7042	NA	6415	6350[c]
	I_1, km/mol	33.2	33.4	27.0	NA
$HONO_2$					
	ω_1, cm^{-1}	3753	NA	3560	3550
	I_1, km/mol	95.4	88.6	73.2	75[b]
	$2\omega_2$, cm^{-1}	NA	NA	3436	3406
	I_{2v2}	NA	NA	2.2	1.7[b]
	$I_{1,HONO2}/I_{1,HOONO}$	2.87	2.65	2.71	

a.Bean et al. [7]
b.Chackerian et al. [22]
c. Fry et al. [55]

The branching ratio from reaction 3.1, k_{1b}/k_{1a}, was therefore calculated from each measured spectrum by

$$\mathrm{BR} = \frac{k_{1b}}{k_{1a}} = \frac{\int Abs_{\mathrm{HOONO}}}{\int Abs_{\mathrm{HONO_2}}} \times E_{\mathrm{HONO_2}} \times f_{Boltz} \times \frac{I_{\mathrm{HONO_2}}}{I_{\mathrm{HOONO}}}. \qquad \text{Equation 3.1}$$

3.3 Results

3.3.1 CRDS Data

Typical CRDS spectra of the products of reactions 3.1-3.5 following excimer photolysis are shown in Figure 3.10 and Figure 3.11. Spectra shown were collected with a photolysis-probe delay of 1 ms and with a pressure of 200 torr. The background CRDS signal with the excimer off has been subtracted and the resulting signal has been converted to units of absorbance per pass. Figure 3.10 shows the spectrum of products formed using H_2 as the OH precursor. Features due to $HONO_2$, HOONO and HONO are all clearly identifiable.

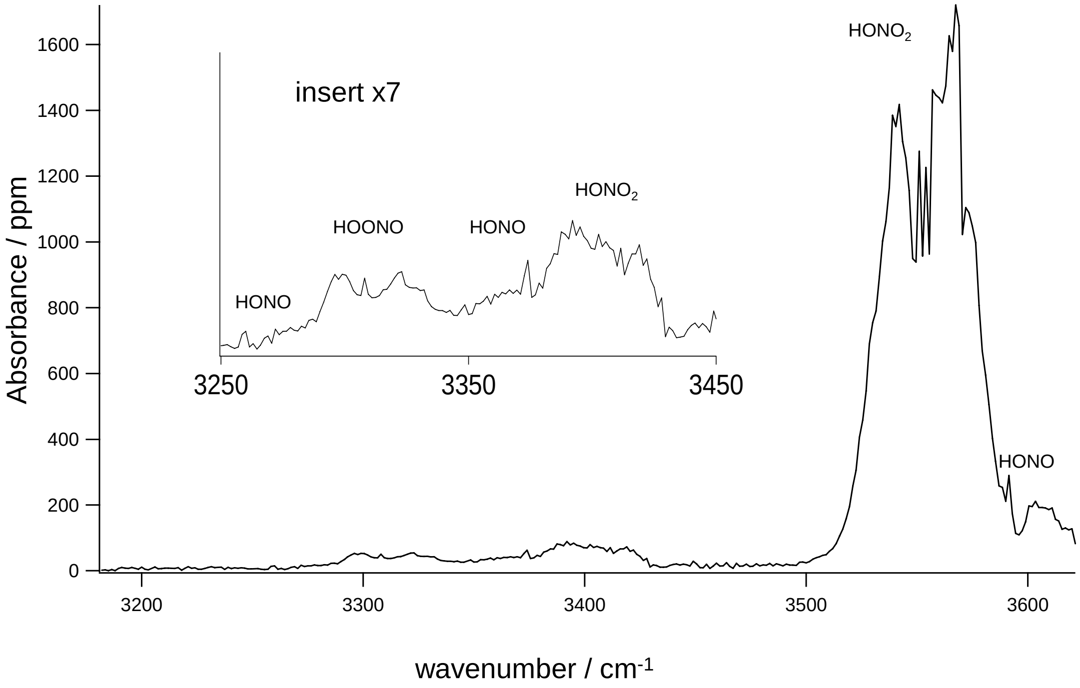

Figure 3.10. IR-CRDS spectrum of the products of the reaction OH + NO_2 using $O(^1D) + H_2$ as the OH source. The spectrum shown has the background with the no excimer photolysis subtracted and has been converted to absorbance units assuming L_{cav} = 50 cm and L_s = 6 cm.

Figure 3.11 shows the spectrum of products formed using CH_4 as the OH precursor. In addition to the features present in Figure 3.10, a peak due to formaldehyde (CH_2O) is also clearly visible. The signal-to-noise ratio for HOONO in Figure 3.11 is worse than in Figure 3.10. This is largely because the total OH yield is lower due to the absence of secondary OH formation via reaction 3.4, thus decreasing the concentration of products. Background absorption of CH_4 to the red of HOONO also acts to increase the noise in the subtracted spectra.

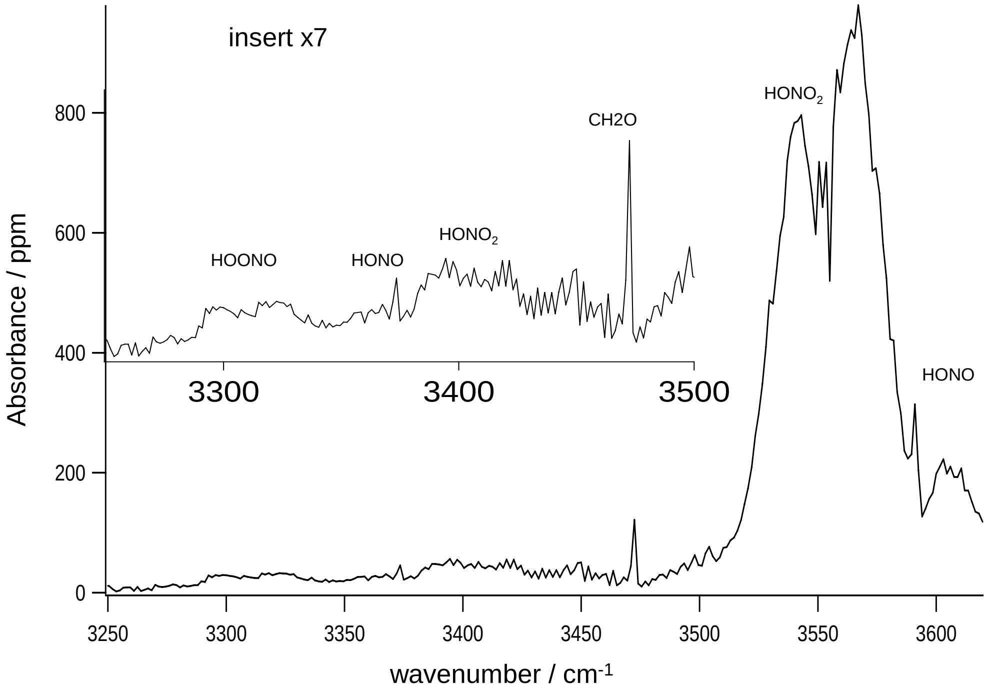

Figure 3.11. IR-CRDS spectrum of the products of the reaction OH + NO_2 using $O(^1D) + CH_4$ as the OH source. The spectrum shown has the background with the no excimer photolysis subtracted and has been converted to absorbance units assuming L_{cav} = 50 cm and L_s = 6 cm.

The signal-to-noise ratios in the spectra shown above were typical for most data. Data taken above 700 torr had more noise. This was symptomatic of a general degradation of the sensitivity of our apparatus under these conditions. Because our mirrors seal to the flow tube by pressing against an O-ring, the alignment of the mirrors depended upon the pressure gradient across the mirrors. For experiments near 1 atm, this pressure gradient did not exist and the optical cavity became unstable. Data taken with SF_6 as a bath gas were also quite noisy, presumably due to aerosols present in the SF_6. An example spectrum with SF_6 is shown in Figure 3.12. The data shown were taken with 330 torr total pressure and 200 torr SF_6. We see that the general features of the component spectra are still discernable, but much noisier.

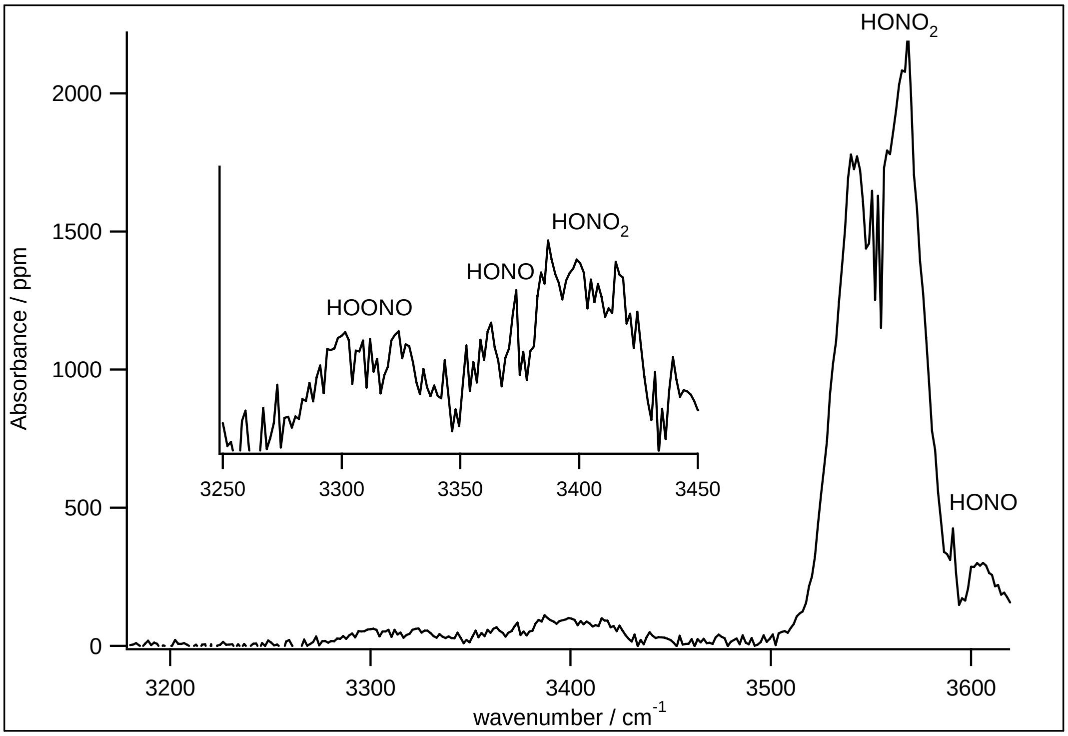

Figure 3.12. IR-CRDS spectrum of the products of the reaction OH + NO_2 using $O(^1D)$ + H_2 as the OH source and with 200 torr SF_6 added as a bath gas. The spectrum shown has the background with the no excimer photolysis subtracted and has been converted to absorbance units assuming L_{cav} = 50 cm and L_s = 6 cm.

3.3.2 Fits and Integration

HOONO and $HONO_2$ absorbances were obtained by scaling reference spectra to fit their ν_1 bands in our data spectra. Due to spectral congestion, reference spectra for the HONO bands and other nitric acid bands in this region were also used in the fits. The reference spectra used are shown in Figure 3.13. The reference spectra were all collected using our CRDS apparatus so that the instrument resolution would be identical. Reference spectra were mapped onto one *x*-axis so they could be summed and compared to the observed spectra.

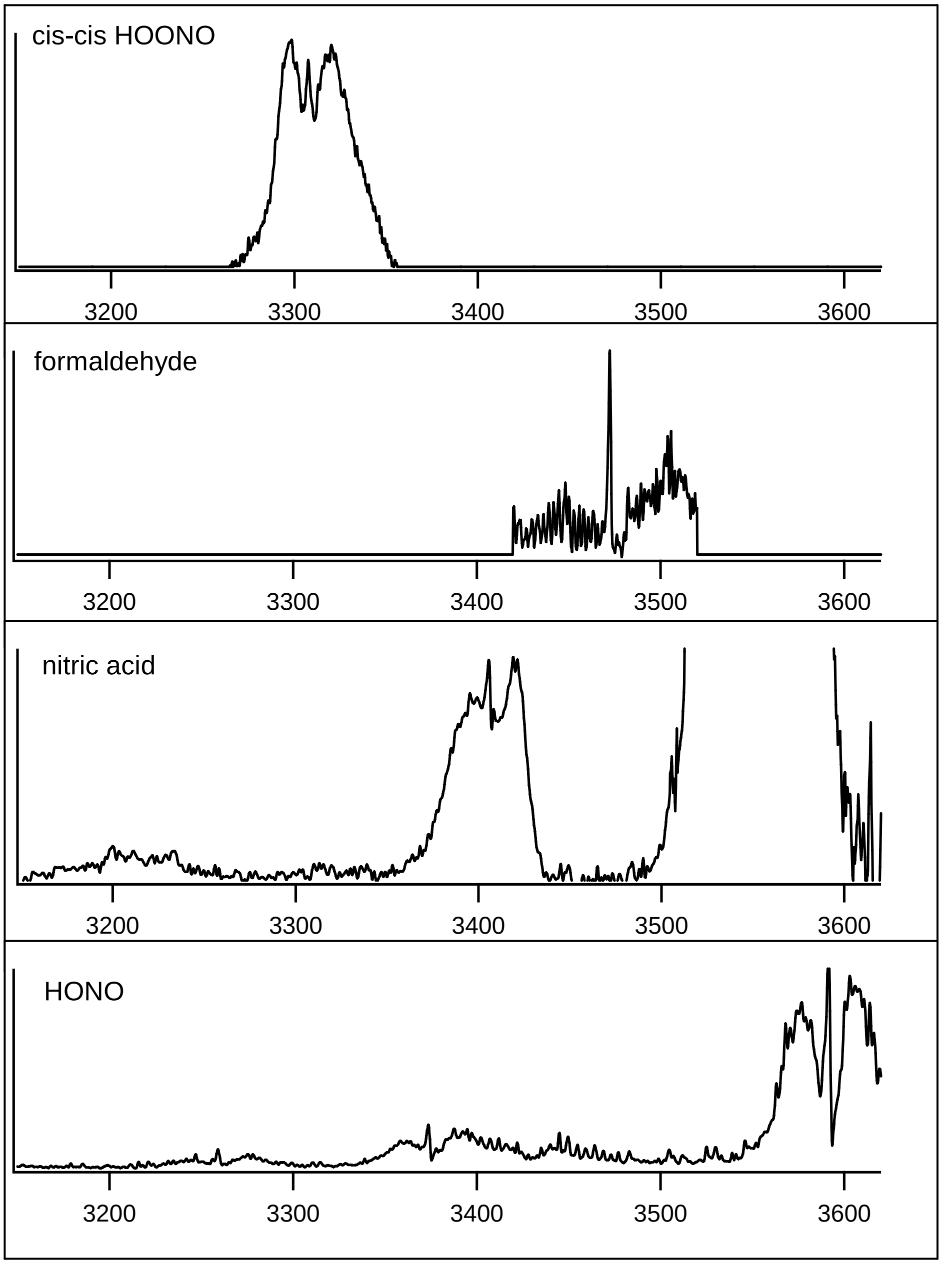

Figure 3.13. Reference spectra used to fit measured CRDS product spectra.

The details of how these spectra were generated are included elsewhere in this thesis. The HOONO reference spectrum was taken from the work described in Bean et al. [7]. The nitric acid reference spectrum was taken from the work described in Chapter 2. The nitric acid ν_1 band, off scale in Figure 3.13, was scaled independently from the other nitric acid peaks. Several ν_1 $HONO_2$ reference spectra were used to account for variation in peak shape with pressure. No other peaks demonstrated a noticeable variation in shape with pressure, indicating that the CRDS artifacts observed for the ν_1 $HONO_2$ band were negligible for the other observed bands.

Using an automated least-squared program to scale the reference spectra was found to be unreliable. Presumably this method failed due to the large stepsize of our data spectra and small shifts in our experimental *x*-axis. As a result, fitting of observed spectra was accomplished by manually scaling reference spectra using IGOR. Fitting of the $HONO_2$ and HOONO peaks were done separately.

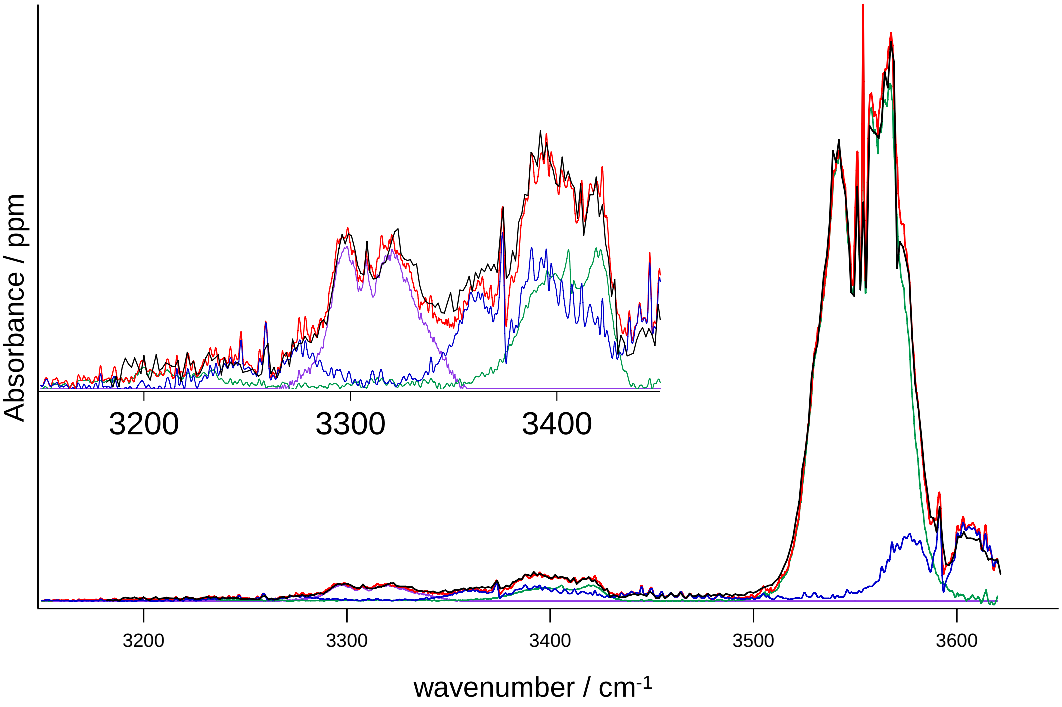

Figure 3.14. CRDS spectrum of photolysis products (black), fit with spectral components due to $HONO_2$ (green), HONO (blue), and HOONO (purple). The sum of the various components is shown in red.

Fitting of the HOONO spectrum was done by focusing on the region from 3150 to 3500 cm^{-1}. A sample fit for this region is shown in Figure 3.14. The fitting was generally done with the following procedure. First the nitric acid spectrum was scaled to fit the $2\nu_2$ band around 3420 cm^{-1}. Second, the HONO spectrum was scaled to fit the $2\nu_2$ bands. Generally, scaling to the P-branch of *cis*-HONO (3230 cm^{-1}), with the least interference from other species, provided a good fit to HONO throughout the spectrum. At this point, the signal to the red of *cis*-HONO was checked for a nonzero baseline. Typical baseline offsets were small, $(1/\tau-1/\tau_0)_{3180} \approx 2000$, relative to the spectral features, $(1/\tau-1/\tau_0)_{3300} \approx 15000$. If needed, a constant was added to the data spectrum to compensate for the offset and then the $HONO_2$ and HONO spectra were re-scaled.

The HOONO spectrum was then scaled to match the data spectrum from 3285 to 3335 cm^{-1}. Small adjustments were then made to the HONO and HOONO spectra to get the best match between the simulated and data spectra. For all spectra it was possible to get the simulated and experimental spectra to match for the HOONO P- and Q-branches as well as the red side of the R-branch. The fits were uniformly poor, however, in the region to the blue of the HOONO R-branch, as will be discussed below (section 3.3.3). The HOONO absorbance was then obtained by having IGOR integrate the HOONO reference spectrum from 3250 to 3350 cm^{-1} using the "print areaxy" command.

The procedure for fitting the nitric acid ν_1 peak focused on the region from 3480 to 3620 cm^{-1}. In this case, the only significant spectral interference was the ν_1 peak of HONO and so only the $HONO_2$ and HONO reference spectra were scaled. As described in Chapter 2, the observed ν_1 band shape changes with pressure. Therefore, each data spectrum was fit with a nitric acid ν_1 reference spectrum taken at a similar pressure.

Typically, the HONO spectrum was scaled first to match the observed signal at 3610 cm^{-1}. The nitric acid spectrum was then scaled to get the best fit throughout the P- and R-branches. The Q-branch could not be reliably used due to the small number of points sampling this region in our data spectra. Unlike in the HOONO region, baseline offsets had a negligible influence on fits to the much larger $HONO_2$ peaks. Once the best fits had been achieved, the $HONO_2$ absorbance was obtained by having IGOR integrate the $HONO_2$ reference spectrum from 3480 to 3620 cm^{-1} using the "print areaxy" command.

This fitting procedure, while not time efficient, yielded good fits to all data. Possible sources of uncertainty in our derived absorbances (assuming no errors in our reference spectra) were noise in our data spectra, spectral congestion, baseline offsets, and judgment errors on the part of the fitter. Noise and spectral congestion will be discussed for HOONO only, since these were negligible sources of uncertainty in the $HONO_2$ absorbance. The typical signal-to-noise ratio for the P-branch of our HOONO data spectrum was ≈ 10 (2σ). The region used to set the HOONO scaling included 30 points. If we assume our noise scales as $N^{-1/2}$, then our signal-to-noise for the fit region as a whole was ≈ 55. This leads to an uncertainty of 2% (2σ).

Uncertainty due to spectral overlap was minimized due to the weighting of HOONO fits toward the P-branch. In this case, only the $2\nu_2$ band of *cis*-HONO impacted the HOONO absorbance. The sensitivity of our HOONO absorbance to the HONO band was evaluated by re-fitting data spectra with different HONO scaling. Due to the small amount of spectral overlap, varying the HONO scaling by ±20% yielded a negligible change in the best-fit HOONO scaling. The uncertainty in our HONO scaling is on the same order as the uncertainty in HOONO (≈5%) and thus spectral congestion from HONO makes a negligible contribution to the overall uncertainty in our HOONO fits.

Evaluating the uncertainty from correcting baseline offsets is difficult, in large part, because the source of these offsets is still not understood. Offsets only appeared when the ozone absorber was present and appeared to be constant over the range scanned. The offsets could be positive or negative and therefore were unlikely due to absorption by an unknown secondary product. The magnitude of the offsets varied from day to day, implying that cavity alignment may have had some impact. My guess is that some photoaccoustic or heating effect caused a small variation in the cavity when the excimer was on. The resulting small change in the "excimer on" ringdowns relative to the "excimer off" ringdowns led to $1/\tau$ values that could be either larger or smaller. If we assume that adding a constant to each data spectrum to account for its offset was valid, then a similar uncertainty analysis to that described in the previous paragraph yields an uncertainty from the baseline correction of about 5% for data with the largest offsets.

This fitting procedure relied on my judgment rather than a least-square analytical function. While every attempt was made to obtain an optimal fit, it is possible personal bias on my part introduced further error. An attempt to quantify this error was made by making the largest and smallest fits I would deem "reasonable." When compared to my "best" fit values, the full range of reasonable fits typically spanned only ±5%. For particularly noisy spectra, this could be as large as ±10%. This is similar to the uncertainty expected based on the noise of the spectra discussed above. It is possible that some component of this error should be treated as systematic. For example, perhaps my eye systematically gives more weight to noise above the mean signal. My re-analysis of the fits showed no evidence of this, however, and so this was treated as a random uncertainty.

The total uncertainty in an individual branching ratio measurement from fitting spectra can be estimated by combining all of the uncertainties discussed above: noise in the data spectra, spectral interference, baseline correction, and judgment errors. I have assumed these uncertainties were random and uncoupled and therefore added them in quaduture. An estimate of the uncertainty in a single branching ratio measurement from the spectral fitting was 7%-11% depending on the amount of noise in the HOONO region.

3.3.3 Stretch-Torsion Coupling

The relative populations in the ground state, P_{Rel}, were calculated from the data in table 3.3 assuming a Boltzmann distribution,

$$P_{\mathrm{Rel}} = \exp\left(\frac{-(E - ZPE)}{k_{\mathrm{B}} * T}\right).$$

The blue shift of each sequence band was calculated by comparing the ν_1=1←0 transition frequencies for states with torsional excitation to the transition frequency of the ground state.

The partition function, Q,

$$Q = \sum_{\text{all states}} P_{\mathrm{Rel}} = 1.64,$$

was used calculate what fraction of the total ν_1=1←0 absorbance is included in the HOONO reference spectrum used for integration.

$$f_{included} = \frac{\sum_{\text{included states}} P_{\text{Rel}}}{Q}$$

Our measured *cis-cis* HOONO absorbances can then be corrected to represent the total HOONO ν_1 absorption through a simple correction factor,

$$Abs_{\text{true}} = Abs_{\text{obs}} * \left(\frac{1}{f_{\text{included}}} \right) = Abs_{\text{obs}} * F_{Boltz} .$$

From looking at the blue shifts in Table 3.2, for most sequence bands it is clear whether or not they qualify as “included states” for our calculation of f_{included}. In addition to the fundamental, the first two states with population only in ν_8 clearly do not shift the absorption frequency outside our reference HOONO spectrum. Most other states clearly do. The two states that are unclear are the first HOON torsion (ν_9=1,ν_8=0), and the first combination band (1,1). The predicted blue shifts of these bands of about 45 cm^{-1} places them right at the edge of HOONO reference spectrum. This can be seen graphically in Figure 3.15.

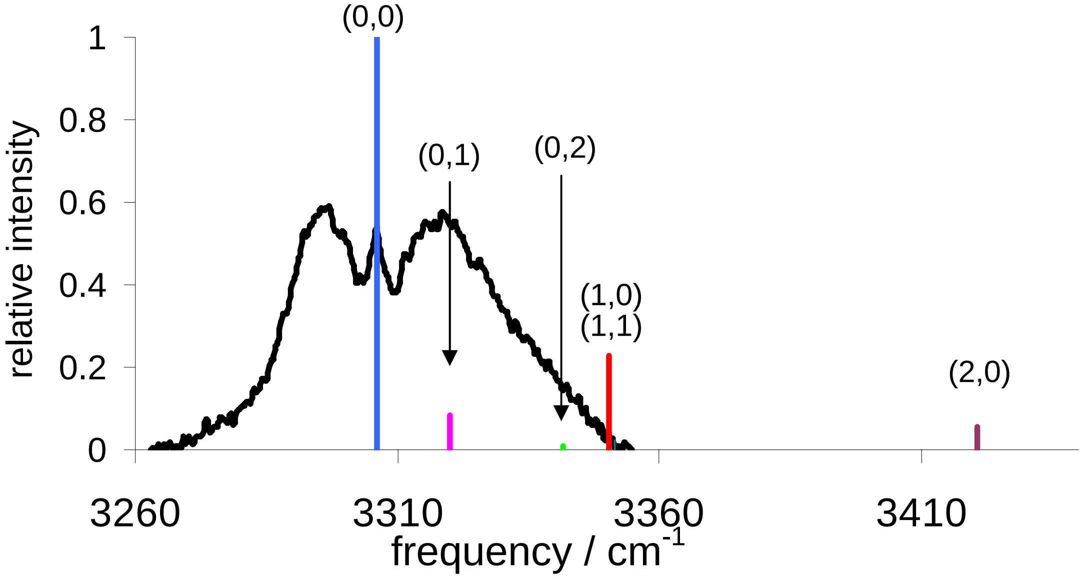

Figure 3.15. Positions and relative intensities of the lowest calculated HOONO OH stretch transitions with population in torsional modes. Transitions are labeled with the number of torsional quanta as (ν_9, ν_8). The HOONO spectrum used to fit our CRDS product spectra is shown for comparison.

Pending a more detailed spectroscopic analysis, three values of F_{Boltz} were calculated. The lower limit of 1.21 was obtained assuming (1,0) and (1,1) were fully contained within our reference spectrum. The upper limit of 1.48 was obtained assuming those two sequence bands were completely outside our reference spectrum. It is likely that some fraction of these bands was included in our reference spectrum and that F_{Boltz} lies between these limits. Assuming that half of those two states was accounted for by our reference HOONO spectrum yields $F_{\mathrm{Bolt}} = 1.33$.

This correction factor is larger than that derived from the two-dimensional picture (1.25) that only looked at the influence of ν_9. This increase has two sources: (1) the energies of the lowest ν_9 states are lower, leading to a greater population in states that cause large blueshifts and (2) combination bands add new populated states that have significant blueshifts.

We now look at the more recent attempt to measure the HOONO spectrum, including the intensity to the blue. Figure 3.16 shows the three spectra taken for this purpose (0.2 cm^{-1} stepsize) along with the average of the three. Figure 3.17 shows the fit to this spectrum used to subtract contributions from HONO and HONO$_2$. The residual, presumably the spectrum of HOONO, is shown offset in the upper portion of Figure 3.17. We see outside the main *cis-cis* HOONO peak there is clearly spectral intensity around 3370 cm^{-1} that cannot be subtracted out with either HONO or HONO$_2$. Using this new HOONO spectrum to re-fit branching ratio data led to consistently better fits in the region to the blue of HOONO (see example in Figure 3.18).

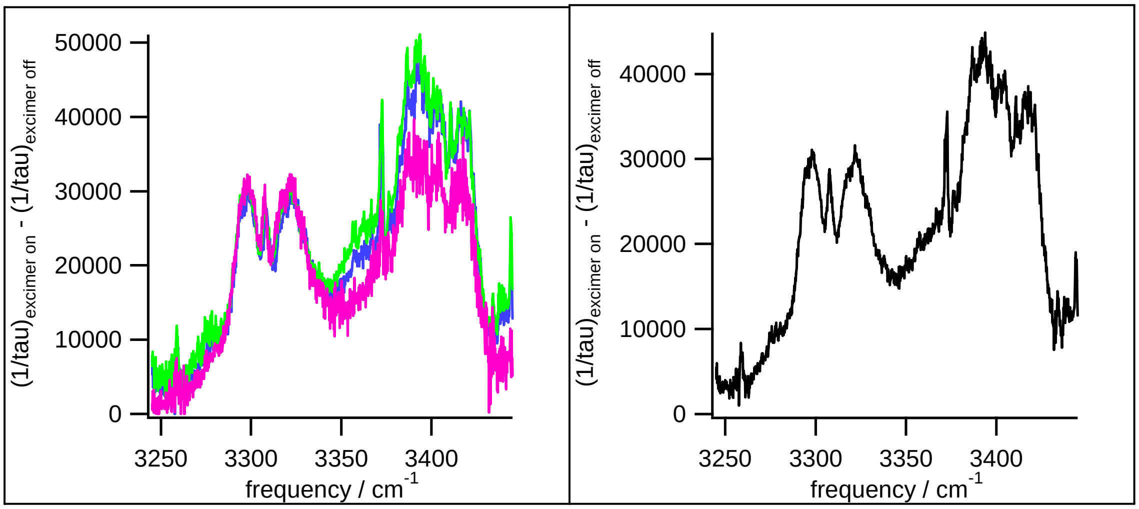

Figure 3.16. Three spectra used to search for spectral features due to torsionally-excited HOONO. Spectra shown were taken at 0.2 cm^{-1} step size and have the background without photolysis subtracted. The average of the three spectra is shown on the right.

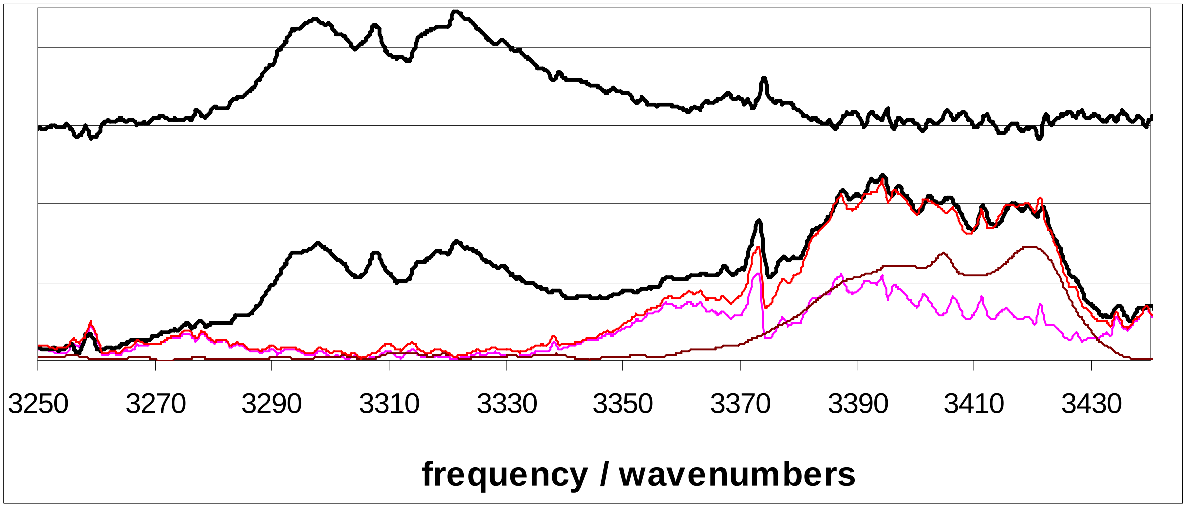

Figure 3.17. Average product spectrum from Figure 3.16 (black) shown along with reference spectra used for subtraction of HONO (pink) and $HONO_2$ (brown). The sum of the fit spectra are shown in red. The residual, presumably the spectrum of HOONO, is shown above.

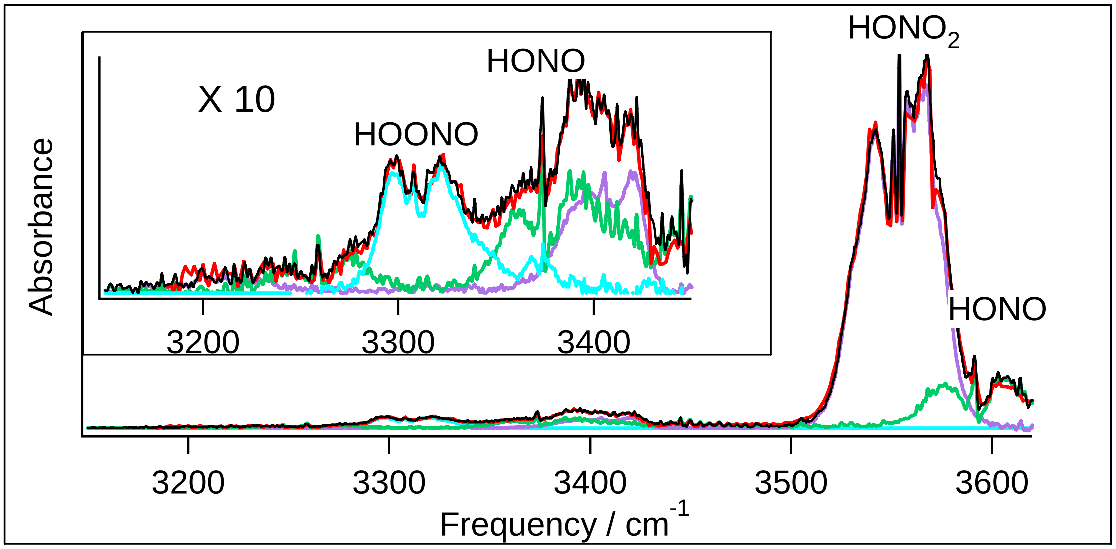

Figure 3.18. Re-fit of some branching ratio data (red) usng the new HOONO spectrum (blue) along with reference spectra for $HONO_2$ (purple), and HONO (green). The sum of these spectra (black) match the observed spectrum well at all frequencies.

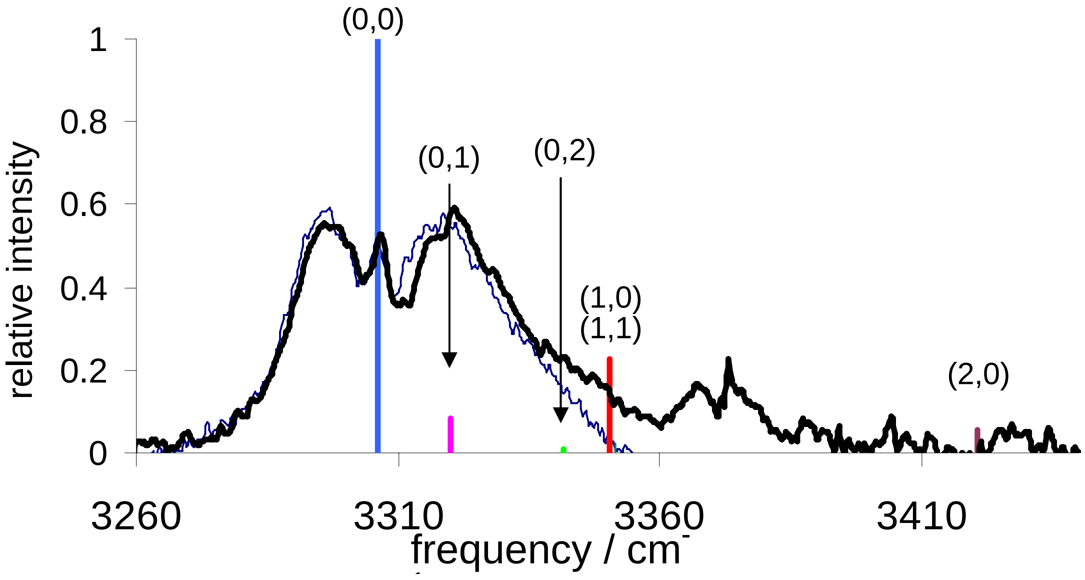

Figure 3.19. New measured HOONO spectrum from Figure 3.17 (thick line) compared with positions and relative intensities of the lowest calculated HOONO OH stretch-torsion transitions. Transitions are labeled with the number of torsional quanta as (ν_9, ν_8). The HOONO spectrum used to fit our CRDS product spectra is shown for comparison (thin line).

The newly measured HOONO spectrum is shown along with the positions of the calculated transitions of torsionally excited HOONO in Figure 3.19. We still do not capture any transitions shifted above 3380 cm^{-1}. The shape from 3250 to 3380 cm^{-1} indicates that the new spectrum includes the (1,0) and (1,1) sequence bands that were the largest source of uncertainty in our derivation of F_{Boltz} above. The ratio of integrated absorbance for the two HOONO spectra is $A_{\mathrm{new}}/A_{\mathrm{old}} = 1.20$. If we assume that the (2,0) state and all others shifted more than this state are not included in the new spectrum, then our correction factor becomes

$$F_{Boltz} = \frac{A_{\mathrm{new}}}{A_{\mathrm{old}}} * \left(\frac{\sum_{(0,0)\text{-}(1,1)} P_{\mathrm{Rel}}}{Q} \right) = 1.20 * 1.21 = 1.45 .$$

If instead the (2,0) state is included in the new spectrum this would decrease to 1.37. This 5% change gives an estimate of the uncertainty in this correction factor. These numbers are in good agreement with *ab initio* correction factors calculated without using the new spectrum. My best estimate of the correction factor is F_{Boltz}=1.41±0.07.

3.3.4 Branching Ratio

As described above, the branching ratio for each spectrum was calculated with eq 3.1.

$$\mathrm{BR} = \frac{k_{1b}}{k_{1a}} = \frac{\int Abs_{\mathrm{HOONO}}}{\int Abs_{\mathrm{HONO_2}}} \times E_{\mathrm{HONO_2}} \times F_{Boltz} \times \frac{I_{\mathrm{HONO_2}}}{I_{\mathrm{HOONO}}} = \frac{\int Abs_{\mathrm{HOONO}}}{\int Abs_{\mathrm{HONO_2}}} \times E_{\mathrm{HONO_2}} \times 1.41 \times 2.71$$

where $E_{\mathrm{HONO_2}}$ is the pressure-dependent correction to the nitric acid absorbance, F_{Boltz}=1.41 is the correction for torsionally excited HOONO, and the ratio of integrated cross sections $I_{\mathrm{HONO2}}/I_{\mathrm{HOONO}}$ has been calculated to be 2.71. The raw data and corrections leading to the individual branching ratio measurements are shown in Table 3.4. A plot of the full data set of branching ratios as a function of pressure is shown in Figure 3.20.

Table 3.4. Pressures, areas, and correction factors used to calculate branching ratios. Pressures are in Torr, areas are from integrated spectra in ($1/\tau$-$1/\tau_0$).

Date	scan	OH source	Pbar	Peff	HOONO area	$HONO_2$ area	E_{HONO2}	BR
17-Aug-05	2	H2	25	17.6	3.30E+05	1.41E+07	2.32	0.039
17-Aug-05	1	H2	25	17.6	2.73E+05	1.41E+07	2.32	0.032
11-Aug-05	6	H2	25	19.4	5.12E+05	2.13E+07	2.29	0.040
11-Aug-05	1	H2	25	19.5	3.50E+05	2.03E+07	2.28	0.029
11-Aug-05	4	H2	25	20.9	4.65E+05	2.24E+07	2.26	0.035
22-Aug-05	11	H2	35	26.3	6.63E+05	2.11E+07	2.19	0.055
22-Aug-05	13	H2	35	26.3	5.30E+05	2.21E+07	2.19	0.042
17-Aug-05	6	H2	50	32.2	6.04E+05	2.37E+07	2.13	0.046
17-Aug-05	5	H2	50	39.3	7.55E+05	2.42E+07	2.07	0.058
11-Aug-05	7	H2	50	40.7	7.33E+05	2.58E+07	2.06	0.053
11-Aug-05	2	H2	50	40.9	5.49E+05	2.34E+07	2.05	0.044
17-Aug-05	3	H2	75	53.7	6.60E+05	2.23E+07	1.97	0.057
17-Aug-05	4	H2	75	53.7	7.99E+05	2.54E+07	1.97	0.061
3-May-05	10	H2	70	54.0	5.98E+05	2.09E+07	1.97	0.056

11-May-05	9	CH4	57.4	57.4	4.68E+05	1.39E+07	1.95	0.066
11-Aug-05	3	H2	75	59.0	6.64E+05	2.69E+07	1.94	0.049
2-Mar-05	10	H2	71	64.1	1.12E+06	4.55E+07	1.91	0.049
11-Aug-05	10	H2	75	65.0	7.79E+05	3.10E+07	1.91	0.050
14-Apr-05	1	H2	95	71.3	7.87E+05	2.33E+07	1.88	0.068
2-May-05	13	H2	100	73.9	6.49E+05	2.28E+07	1.87	0.058
2-May-05	9	H2	100	74.4	5.82E+05	1.93E+07	1.87	0.062
2-May-05	10	H2	100	74.4	5.41E+05	1.81E+07	1.87	0.061
2-May-05	14	H2	100	74.6	5.92E+05	2.11E+07	1.87	0.057
2-May-05	8	H2	100	76.0	9.31E+05	3.29E+07	1.86	0.058
9-May-05	5	H2	100	76.2	5.34E+05	2.05E+07	1.86	0.053
2-May-05	15	H2	100	78.2	7.10E+05	2.78E+07	1.85	0.053
9-May-05	6	H2	100	78.6	5.23E+05	1.99E+07	1.85	0.054
17-Aug-05	7	H2	100	79.9	8.00E+05	2.52E+07	1.85	0.066
17-Aug-05	8	H2	100	79.9	8.00E+05	2.45E+07	1.85	0.068
11-May-05	8	CH4	80	80.0	6.51E+05	1.93E+07	1.85	0.070
2-May-05	7	H2	100	80.1	9.13E+05	3.13E+07	1.85	0.060
2-May-05	16	H2	100	80.5	9.70E+05	3.68E+07	1.84	0.055
9-May-05	4	H2	100	81.3	6.95E+05	2.42E+07	1.84	0.060
9-May-05	1	H2	100	81.5	4.71E+05	1.25E+07	1.84	0.078
2-May-05	5	H2	100	81.9	6.68E+05	2.37E+07	1.84	0.059
2-May-05	6	H2	100	81.9	6.81E+05	2.37E+07	1.84	0.060
2-May-05	3	H2	100	82.0	6.99E+05	2.52E+07	1.84	0.058
2-May-05	4	H2	100	82.0	6.68E+05	2.39E+07	1.84	0.058
2-May-05	2	H2	100	82.0	6.99E+05	2.52E+07	1.84	0.058
2-May-05	1	H2	100	82.2	7.76E+05	2.65E+07	1.84	0.061
9-May-05	7	H2	100	84.4	7.48E+05	2.43E+07	1.83	0.064
9-May-05	2	H2	100	84.6	7.24E+05	2.62E+07	1.83	0.058
9-May-05	3	H2	100	84.6	5.79E+05	1.83E+07	1.83	0.066
3-May-05	1	H2	100	86.6	7.48E+05	2.21E+07	1.82	0.071
11-Aug-05	8	H2	100	89.7	8.79E+05	2.96E+07	1.81	0.063
11-Aug-05	9	H2	100	91.1	6.73E+05	2.49E+07	1.81	0.057
30-Mar-05	13	H2	103	94.6	5.30E+05	1.84E+07	1.79	0.062
16-Feb-05	17	H2	100	96.0	5.89E+05	1.66E+07	1.79	0.076
22-Apr-05	4	CH4	100	100.0	9.05E+05	2.84E+07	1.78	0.069
22-Apr-05	7	CH4	100	100.0	4.50E+05	1.19E+07	1.78	0.081
22-Apr-05	6	CH4	100	100.0	8.77E+05	2.76E+07	1.78	0.068
22-Apr-05	5	CH4	100	100.0	7.30E+05	2.33E+07	1.78	0.067
20-Apr-05	5	CH4	102	102.0	9.62E+05	3.04E+07	1.77	0.068

20-Apr-05	6	CH4	102	102.0	9.62E+05	2.76E+07	1.77	0.075
14-Apr-05	10	H2	150	102.4	1.07E+06	4.00E+07	1.77	0.058
14-Apr-05	7	H2	200	111.4	1.02E+06	2.99E+07	1.74	0.075
11-May-05	1	CH4	116	116.0	5.91E+05	1.60E+07	1.73	0.082
2-Mar-05	17	H2	151.4	148.3	8.40E+05	2.62E+07	1.65	0.074
10-Aug-05	1	H2	200	150.4	1.26E+06	4.06E+07	1.65	0.072
10-Aug-05	2	H2	200	151.4	1.39E+06	4.68E+07	1.65	0.069
10-Aug-05	3	H2	200	151.4	1.05E+06	3.28E+07	1.65	0.074
10-Aug-05	4	H2	200	151.5	8.74E+05	2.53E+07	1.65	0.080
10-Aug-05	6	H2	200	152.2	1.37E+06	4.26E+07	1.65	0.075
10-Aug-05	5	H2	200	152.7	8.74E+05	2.66E+07	1.64	0.076
3-May-05	6	H2	180	167.5	5.73E+05	1.83E+07	1.62	0.074
6-Oct-05	8	H2	514	169.4	1.89E+06	6.01E+07	1.61	0.075
6-Oct-05	4	H2	515	169.9	1.68E+06	6.04E+07	1.61	0.066
17-Feb-05	17	H2	200	187.6	1.65E+06	4.85E+07	1.58	0.082
30-Mar-05	3	H2	225	192.9	6.40E+05	2.50E+07	1.57	0.062
6-Oct-05	6	H2	513	193.6	2.36E+06	7.19E+07	1.57	0.080
11-Oct-05	11	H2	510	196.1	2.03E+06	5.95E+07	1.57	0.083
18-Apr-05	6	CH4	200	200.0	7.66E+05	2.47E+07	1.56	0.076
11-May-05	12	CH4	200	200.0	7.69E+05	1.91E+07	1.56	0.098
18-Apr-05	3	CH4	200	200.0	1.01E+06	3.34E+07	1.56	0.074
18-Apr-05	1	CH4	200	200.0	9.60E+05	2.97E+07	1.56	0.079
18-Apr-05	4	CH4	200	200.0	8.06E+05	2.95E+07	1.56	0.067
20-Apr-05	12	CH4	201	201.0	1.00E+06	2.96E+07	1.56	0.083
20-Apr-05	11	CH4	201	201.0	7.35E+05	2.26E+07	1.56	0.080
11-Oct-05	7	H2	505	209.5	2.13E+06	5.38E+07	1.55	0.098
11-Oct-05	13	H2	515	217.6	1.97E+06	5.20E+07	1.53	0.094
11-Oct-05	9	H2	510	219.5	2.57E+06	6.99E+07	1.53	0.092
2-Mar-05	4	H2	230	222.0	1.14E+06	3.90E+07	1.53	0.073
2-Mar-05	7,8	H2	233	224.9	1.33E+06	4.21E+07	1.52	0.079
14-Apr-05	3	H2	300	225.5	1.07E+06	2.83E+07	1.52	0.095
6-Oct-05	3	H2	520	229.3	1.68E+06	5.49E+07	1.52	0.077
11-Oct-05	5	H2	510	232.4	1.91E+06	5.51E+07	1.51	0.087
3-May-05	4	H2	252	237.1	7.96E+05	2.14E+07	1.51	0.094
22-Aug-05	3	H2	350	256.9	8.21E+05	2.26E+07	1.48	0.094
22-Aug-05	1	H2	350	274.7	6.32E+05	1.61E+07	1.46	0.103
29-Aug-05	1-2	H2	500	282.3	1.26E+06	4.03E+07	1.45	0.082
14-Apr-05	5	H2	400	294.7	1.28E+06	3.79E+07	1.44	0.090
6-Oct-05	2	H2	515	304.2	1.68E+06	5.44E+07	1.43	0.083

11-May-05	6	CH4	305	305.0	1.05E+06	2.53E+07	1.43	0.111
20-Apr-05	1	CH4	305	305.0	1.01E+06	2.97E+07	1.43	0.091
20-Apr-05	2	CH4	305	305.0	1.11E+06	3.10E+07	1.43	0.096
11-Oct-05	3	H2	518	335.5	2.27E+06	6.00E+07	1.40	0.103
3-May-05	8	H2	351	335.6	7.17E+05	2.03E+07	1.40	0.097
3-May-05	7	H2	357	335.7	1.20E+06	3.28E+07	1.40	0.100
30-Mar-05	4	H2	405	343.0	2.60E+05	8.93E+06	1.39	0.080
11-Oct-05	8	H2	525	343.0	2.24E+06	5.38E+07	1.39	0.114
30-Mar-05	5	H2	410	347.1	5.20E+05	1.77E+07	1.39	0.081
23-Aug-05	1-3	CH4	350	350.0	1.59E+06	3.80E+07	1.39	0.115
6-Oct-05	5	H2	515	358.5	3.94E+06	9.99E+07	1.38	0.109
2-Mar-05	9	H2	373	363.1	1.76E+06	5.06E+07	1.38	0.097
11-Oct-05	2	H2	520	383.8	2.07E+06	4.96E+07	1.36	0.117
3-May-05	2	H2	408	394.3	9.95E+05	2.35E+07	1.35	0.120
11-May-05	10	CH4	400	400.0	9.48E+05	2.40E+07	1.34	0.112
20-Apr-05	9		400	400.0	1.30E+06	3.26E+07	1.34	0.113
20-Apr-05	10	CH4	400	400.0	1.22E+06	2.91E+07	1.34	0.119
11-Oct-05	6	H2	525	414.1	1.87E+06	4.53E+07	1.33	0.118
29-Aug-05	5-8	H2	500	417.0	1.31E+06	4.02E+07	1.33	0.094
6-Oct-05	7	H2	513	418.3	3.00E+06	7.91E+07	1.33	0.109
11-Oct-05	10	H2	510	423.9	1.76E+06	3.79E+07	1.33	0.134
11-Oct-05	12	H2	515	424.7	1.64E+06	3.72E+07	1.33	0.127
29-Aug-05	9	H2	500	429.6	2.62E+06	6.75E+07	1.32	0.112
6-Oct-05	1	H2	523	431.3	1.68E+06	4.94E+07	1.32	0.098
14-Apr-05	2	H2	510	433.2	1.13E+06	3.20E+07	1.32	0.102
29-Aug-05	11	H2	500	433.3	2.02E+06	6.37E+07	1.32	0.092
29-Aug-05	11	H2	500	433.3	2.43E+06	6.37E+07	1.32	0.111
11-Oct-05	1	H2	515	434.0	1.97E+06	4.13E+07	1.32	0.138
11-Oct-05	4	H2	525	439.5	1.91E+06	4.37E+07	1.32	0.127
29-Aug-05	4	H2	500	447.7	2.56E+06	6.04E+07	1.31	0.124
29-Aug-05	10	H2	500	452.0	2.49E+06	6.09E+07	1.31	0.120
3-May-05	11	H2	490	477.3	8.55E+05	2.04E+07	1.29	0.124
14-Apr-05	6	H2	605	495.4	1.49E+06	3.53E+07	1.28	0.126
11-May-05	2	CH4	501	501.0	6.57E+05	1.45E+07	1.27	0.136
2-Mar-05	12	H2	512	503.1	1.18E+06	2.63E+07	1.27	0.135
20-Apr-05	4	CH4	505	505.0	1.47E+06	3.13E+07	1.27	0.141
20-Apr-05	3	CH4	505	505.0	1.40E+06	3.26E+07	1.27	0.129
2-Mar-05	13	H2	522	510.4	9.80E+05	2.51E+07	1.27	0.118
30-Mar-05	6	H2	610	516.0	1.21E+06	3.28E+07	1.27	0.111

22-Aug-05	6	H2	750	518.6	1.99E+06	4.89E+07	1.26	0.123
30-Mar-05	8	H2	614	519.4	8.96E+05	2.19E+07	1.26	0.124
22-Aug-05	5	H2	750	519.9	2.46E+06	6.05E+07	1.26	0.123
11-May-05	3	CH4	520	520.0	8.17E+05	1.82E+07	1.26	0.136
22-Aug-05	8	H2	750	521.1	1.44E+06	3.72E+07	1.26	0.117
4-Aug-05	4	H2	700	538.3	1.80E+06	3.89E+07	1.25	0.141
4-Aug-05	5	H2	700	538.3	2.15E+06	4.71E+07	1.25	0.139
4-Aug-05	6	H2	700	538.3	2.59E+06	5.70E+07	1.25	0.139
4-Aug-05	3	H2	700	539.0	2.16E+06	5.06E+07	1.25	0.130
14-Apr-05	9	H2	700	565.9	1.33E+06	3.39E+07	1.24	0.121
3-May-05	5	H2	582	566.8	9.55E+05	2.14E+07	1.24	0.138
14-Apr-05	8	H2	700	567.1	1.51E+06	3.72E+07	1.24	0.126
20-Apr-05	13	CH4	605	605.0	1.37E+06	3.28E+07	1.22	0.131
20-Apr-05	14	CH4	605	605.0	1.69E+06	3.62E+07	1.22	0.147
11-May-05	11	CH4	606	606.0	9.49E+05	2.19E+07	1.22	0.136
30-Mar-05	10	H2	730	614.3	1.12E+06	2.80E+07	1.21	0.126
30-Mar-05	11	H2	732	615.8	1.00E+06	2.43E+07	1.21	0.130
3-May-05	9	H2	654	639.4	8.28E+05	1.99E+07	1.20	0.133
14-Apr-05	4	H2	770	639.9	1.50E+06	3.35E+07	1.20	0.143
20-Apr-05	8	CH4	710	710.0	1.44E+06	3.43E+07	1.17	0.137
20-Apr-05	7	CH4	710	710.0	1.62E+06	3.32E+07	1.17	0.160
11-May-05	7	CH4	716	716.0	8.41E+05	1.72E+07	1.16	0.161
23-Aug-05	4-6	CH4	750	750.0	2.10E+06	4.85E+07	1.15	0.144
3-May-05	3	H2	770	752.0	7.96E+05	1.78E+07	1.15	0.149

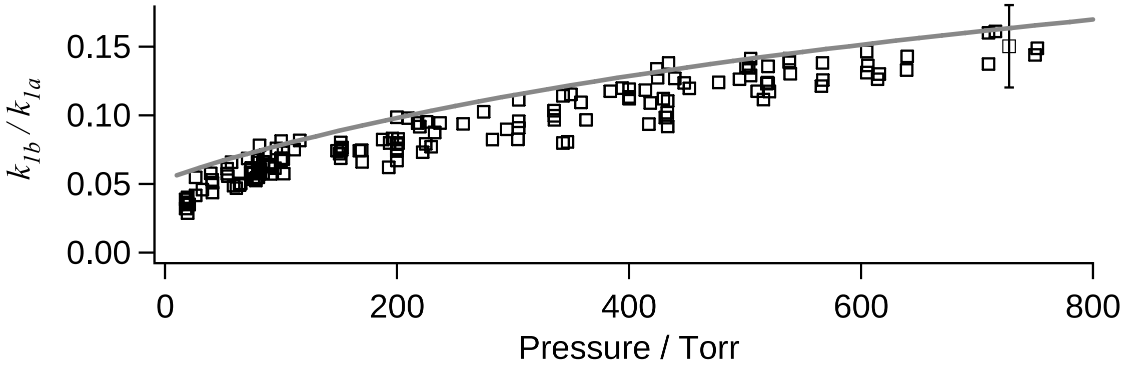

Figure 3.20. Branching ratio data taken as a function of pressure. A representative 2σ error bar has been added to the point at 750 torr. The solid grey line represents the branching ratio obtained from the modeling fit of Golden et al. [49].

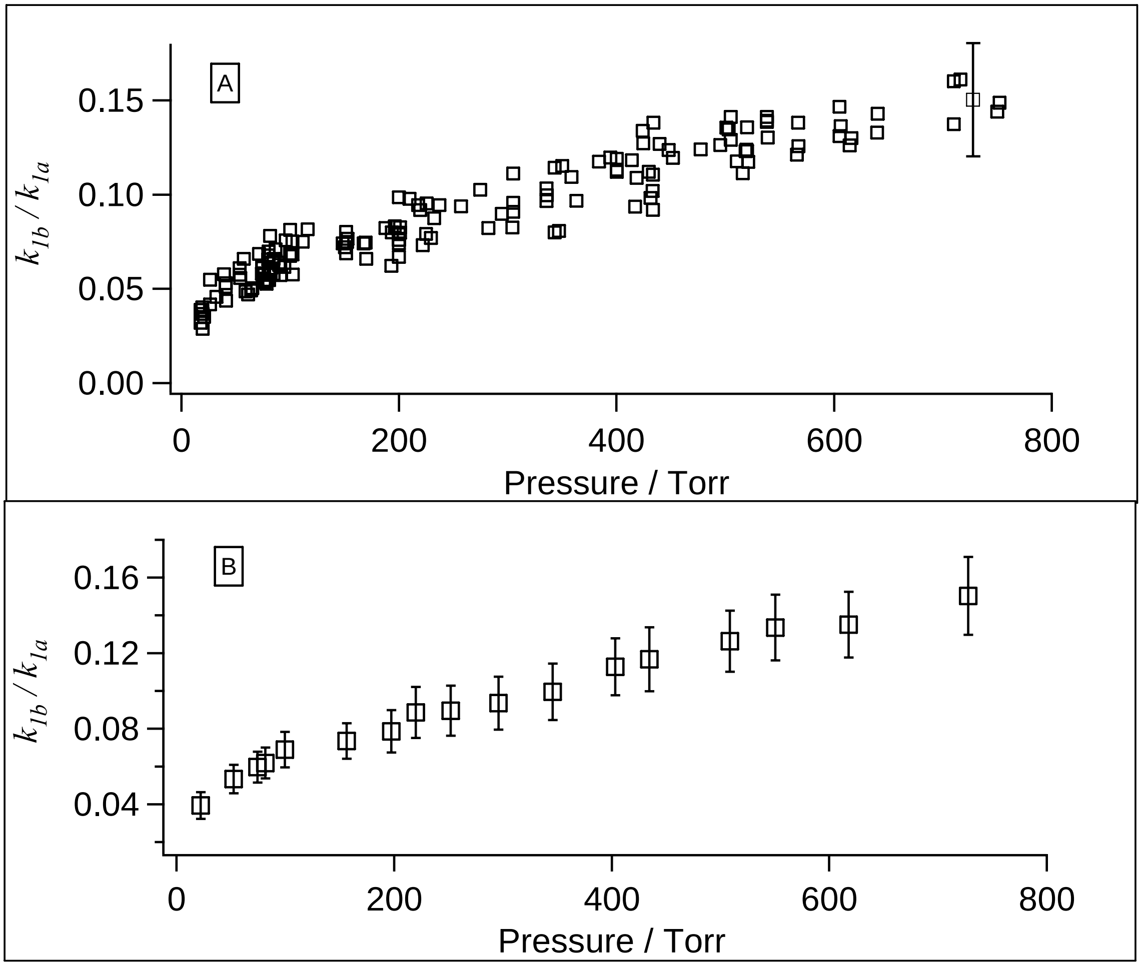

Figure 3.21. Branching ratio data as a function of pressure. All data is shown in (a). A representative 2σ error bar has been added to the point at 750 torr. Data have been binned into groups and averaged in (b).

In addition to the random experimental uncertainty represented by the scatter in the Figure 3.20 data, significant systematic uncertainties exist. The largest of these are uncertainties in the calculated ratio of intensities E_{HONO2} and F_{Boltz}, estimated to be 5% each. These systematic uncertainties have been added to the estimated 7%-11% random uncertainty to give the overall 2σ uncertainty. An error bar representing this uncertainty in a single measurement has been included in Figure 3.21(a). The random uncertainty in the branching ratio at a given pressure is reduced, however, by the large amount of data taken. Figure 3.21(b) shows the average of the data from Figure 3.21(a) binned into several pressure bins. The error bars shown combine the standard deviation of the mean for the data averaged combined with the systematic uncertainties. The HOONO branching ratio varies significantly with pressure, increasing from 0.039 ± 0.008 at 20 torr to 0.150 ± 0.025 at 760 torr.

3.4 Discussion

3.4.1 Comparison With Past Results

3.4.1.1 Stretch-Torsion Coupling

We can compare our calculated torsional energy levels to past calculations using only a 2D potential [45, 46]. The ν_9 energy levels have now been calculated thrice by us and once by Amit Sinha's group, each with slightly different methods. The resulting energies and energies relative to the calculated zero-point energy are shown in Figure 3.22.

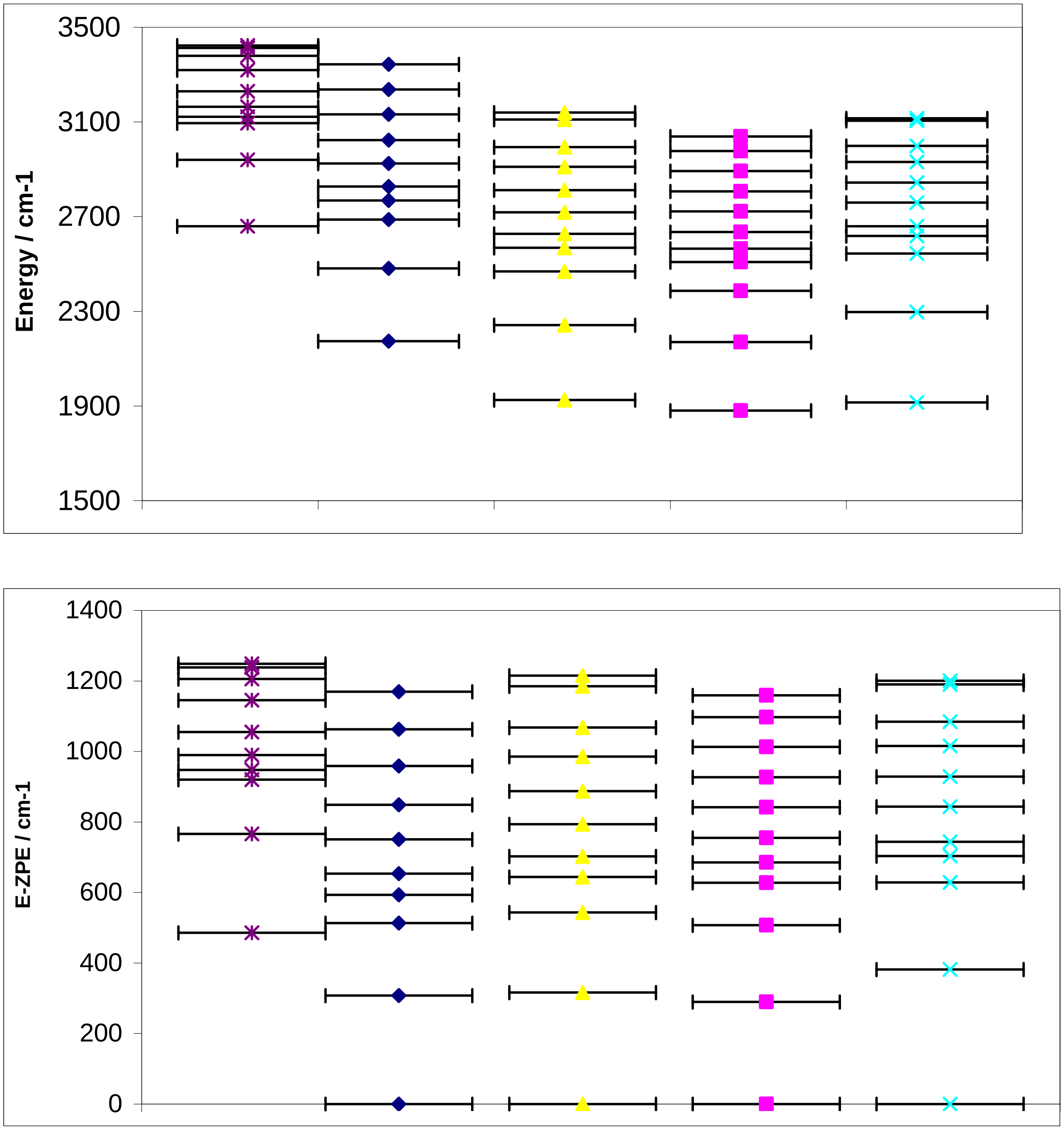

Figure 3.22. Comparison of calculated HOONO torsion energy levels. All results are for v_1=0. From left to right: current results with v_8>0 (purple stars), current results with v_8=0 (blue diamonds), 2D results on minimum energy path along our 3D potential (yellow triangles), 2D calculations from Matthews et al.[45] with heavy atom geometries relaxed (pink squares), and 2D calculations from McCoy et al. with the heavy atoms fixed[46]. The bottom panel shows the energies relative to the zero-point energy.

We see that the relative energies of the v_9 levels when some flexibility of the heavy atoms is included (the middle three sets of points) are very similar. Explicitly adding the coupling to v_8 does not make a large change the v_9 levels relative to those of

Matthews et al. [75]. It does, however, add eight levels with $\nu_8 \neq 0$ less than 1200 cm^{-1} above the ZPE.

I make two observations about the above data: (1) the ν_9 levels from our 3D potential are close to those from the best 2D potentials, even as high as 1200cm^{-1} above the ZPE and (2) above the highest torsional level we currently have from the 3D potential, the McKoy et al. results indicate the levels increase fairly rapidly in energy. Therefore, while we currently have only calculated torsional states up to 1300 cm^{-1} in energy using the 3D potential, we would expect torsional states higher in energy to have rapidly diminishing Boltzmann populations. As a result, we expect our future calculations of higher-energy states to have a negligible impact on the calculations of F_{Boltz} described in Section 3.3.3.

3.4.1.2 Branching Ratio

The most direct comparison of the results presented here are to the results we previously published in Bean et al. [7]. Before this comparison can be made, however, the results presented in Bean et al. must be revised to account for our improved knowledge of the spectroscopy involved. In Bean et al. we assumed $E_{\mathrm{CRDS}} = 0.85$ and included no correction for torsionally excited HOONO absorption. We also now believe the ratio of cross sections to be 5% lower. Revisions of the published data plots are included with a re-print of the original paper in Appendix A. The published value of 0.075±0.020 at 298 K and 20 torr (P_{eff} = 14 torr(N_2)) should be revised to 0.047±0.013. This value and our current measurement of 0.039 ± 0.008 at 20 torr and 298 K agree within the uncertainty of each measurement. We might have expected the adjusted Bean et al. value to be lower than our current measurement due to its lower effective pressure, but it is difficult to evaluate whether this is true given the large uncertainties involved.

Comparisons to other prior measurements are more tenuous. The extreme pressures and temperatures of Hippler et al. make a direct comparison with these results meaningless. We can say that our results qualitatively agree with their measurement of k_{1b}/k_{1a} = 0.15 at 430 K and 5 bar He [60] since we would expect the branching ratio to increase with pressure and decrease with temperature. D'Ottone et al. measured k_{1b}/k_{1a} = 0.10±0.03 at 413 K and 400 torr He [59]. Again it is difficult to make a quantitative comparison, but this result generally agrees with our data.

Our measured pressure-dependence can also be compared to the modeling studies. For ease of comparison, the branching ratio obtained by Golden et al. [49] and Hippler et al. [47] have been superimposed with our data and previous measurements in Figure 3.23.

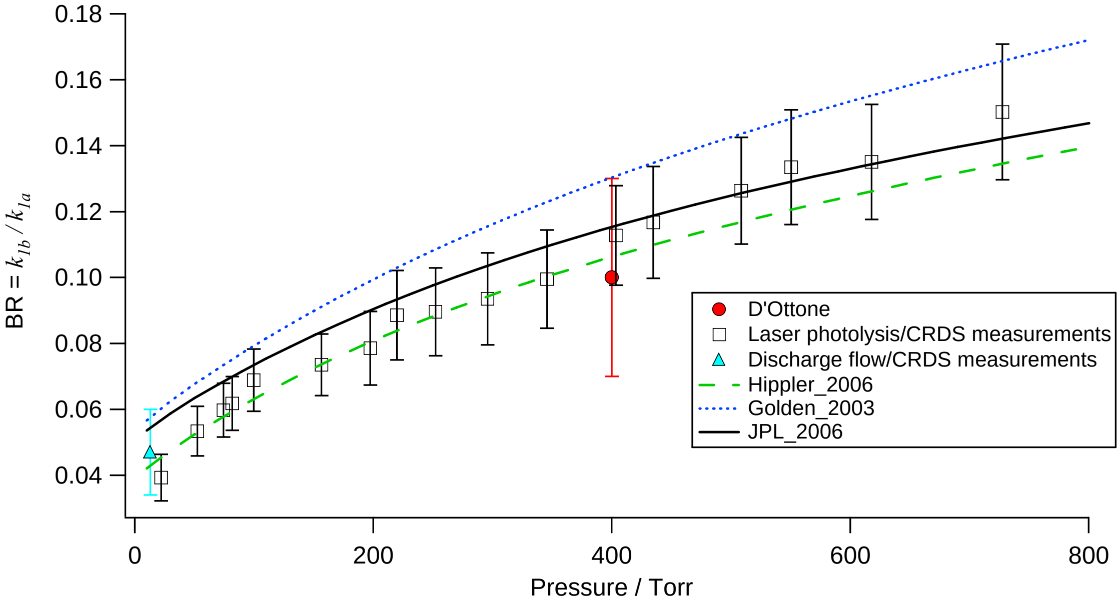

Figure 3.23. Comparison of current branching ratio measurements with prior data from Bean et al. [7] and D'Ottone et al. [59], modeling results from Golden et al. [49] and Hippler et al. [47], and the current JPL kinetics data evaluation.

The general shape of our data agrees with the results of both modeling studies. Our results at low pressure agree better with the results of Hippler et al.. It is unclear whether the published branching ratio in Bean et al impacted the results of Golden et al. and caused their low-pressure branching ratio to be increased. At pressures above 400 torr our data lie between the two modeled results. The older modeling results of Matheu and Green [66] and Troe [67] are qualitatively similar in shape but differ quite substantially in the magnitude of their branching ratios under these conditions. Our measurements above 400 torr actually agree reasonably well with the branching ratio derived from the current JPL data evaluation, although the general shape of the branching ratio over the entire pressure range does not.

3.4.2 Atmospheric Implications

Based on our branching ratio measurements, we recommend a nitric acid yield ($\Phi=k_{1a}/k_{1a}+k_{1b}$) at 1 atm and 298 K of

$$\Phi_{\mathrm{HONO_2}}\left(298\ \mathrm{K},1\ \mathrm{atm}\right)=0.87\pm0.03.$$

Because HOONO redissociates rapidly under atmospheric conditions, the significant HOONO branching ratio we observe acts to lower the critical rate constant k_{1a} and reduce the efficiency of R1 as a sink for HO_x and NO_x. Specifically, k_{1a} should be obtained from measurements of the total rate constant k_1 under these conditions from the expression

$$k_{1a}=\Phi_{HONO_2}\times k_1.$$

This has important implications for our understanding of photochemical smog production. The primary effect of lowering k_{1a} is an increase the lifetime of HO_x and NO_x, resulting in greater ozone production per unit emission of these species. A recent analysis by Martien and Harley evaluated the sensitivity of modeled ozone outputs to nearly 900 model parameters [4]. In their models of 8-hour peak ozone for Rubidoux, CA (east of Los Angeles) they found that the most influential rate constant for ozone production in their model was k_{1a}. The only input parameter with a larger influence on ozone concentrations was the emissions inventory for NO_x.

They calculated a seminormalized sensitivity of modeled ozone to k_{1a} of -50 ppb in polluted areas of eastern Los Angeles [4]. A 13% reduction in k_{1a} due to HOONO production would therefore result in a 7 ppb increase in modeled ozone concentrations. This effect would not be limited to areas of extreme pollution, however. An earlier study by Tonnesen found that a 20% decrease in k_{1a} would result in a 6%-16% increase in ozone concentrations in typical urban conditions and even a 2%-6% increase in ozone concentrations for typical rural conditions [3]. The Tonnesen study also found that a downward adjustment of k_{1a} would change the relative effectiveness of NO_x vs. volatile organic carbon emission control strategies. The direct impact of a 10%-15% HOONO yield on photochemical models would therefore be significant. k_{1a} is also an important parameter in deriving the ozone-forming potentials of hydrocarbons and therefore an adjustment of this value may have secondary impacts upon model outputs.

Another important secondary impact of these branching ratio measurements will be to reduce the uncertainty in the rate constants associated with reaction 3.1a. As discussed above, the two major kinetics data evaluations disagree on the parameters used to describe the pressure dependence of k_{1a} and give large error bars to their parameters. The resulting discrepancy at 1 atm of greater than 10% and the 30% uncertainties are both large for a reaction of such importance. A critical review of photochemical models by Russell and Dennis found that the uncertainty in k_{1a} contributed a significant fraction to the uncertainty in ozone predictions under all conditions [76]. Much of the evaluation uncertainty stems from the prior lack of data on the HOONO branching ratio. The pressure-dependent branching ratio reported here should therefore not only change ozone concentrations from photochemical models, but also reduce this uncertainty in these concentrations.